UNIVERSITY OF CALIFORNIA, SAN DIEGO
Department of Applied Mechanics and Engineering Sciences
La Jolla, California 92093

PLANAR MECHANICS OF FULLY GROUTED CONCRETE MASONRY

by

Robert O. Nunn

Report No. UCSD/AMES/TR-80-001

Prepared for the
National Science Foundation
Grant NSF PFR 78-16581

May 1980

TABLE OF CONTENTS

LIST OF FIGURES

LIST OF TABLES

ACKNOWLEDGMENTS

The experiments that formed the basis of this analysis represent a lot of hard work. The specimens were difficult to construct and handle, and unexpected results were commonplace. Some of those who deserve recognition for their perseverance and cleverness are Don Bowers, Dick Gilbert, Michael Miller, and Chris Farenbaugh.

PLANAR MECHANICS OF FULLY GROUTED CONCRETE MASONRY

by

Robert O. Nunn

Abstract

This report presents data from experiments, and develops a continuum model for the planar behavior of fully grouted concrete masonry. Both unreinforced and reinforced masonry are considered, but otherwise attention is restricted to a single material type.

Data was taken from prisms of several configurations, and from 5-foot square panels cut at an angle relative to the joint system. The panels were tested under direct biaxial stresses, with one edge in tension, and the other in compression or stress-free.

The elastic behavior is found to be quite linear. The form of the elastic law describing this behavior is determined, and the moduli are evaluated. These moduli show substantial anisotropy in stiffness. Hysteresis loops at several load rates are described, and the relation of these loops to the damping of a structure is discussed.

The significance of prism configuration and end conditions, and the relation of prism compressive strength to wall compressive strength are discussed. A law describing the dependence of unreinforced uniaxial tensile strength on direction is presented. This uniaxial law, which shows moderate anisotropy in tensile strength, is incorporated into a law for unreinforced biaxial strength for the special case of principal stresses of opposite sign. A statistical analysis of the biaxial data gives variations in strength that can be expected. The effects of reinforcing on these strength results, and the significance of component strengths, are discussed.

A modified plasticity model describing the behavior of reinforced masonry following initial fracture is presented. The existence of a loading surface is illustrated, and a law is given for the change of this surface based on tensile strain. Tensile strain is also employed in a law describing stiffness degradation. Normality of the plastic strain rate is shown to hold at several points on the loading surface, and a stress rate - total strain rate matrix for plastic behavior is derived.

INTRODUCTION

Masonry is a form of construction that has been practiced for thousands of years. While some traditional materials, such as stone, are rarely used today, concrete block now provides a rapid and economical method of producing structures of one to ten or more stories. The wide variety of brick and block available makes possible buildings of exceptional color and texture.

Though masonry is widely used as a construction material, rather little is known of its properties. Research into its behavior has lagged behind research in other materials. Concrete, for example, has been the subject of careful study by many investigators, and the American Concrete Institute publishes a journal devoted to results of their work. No such journal exists for the publication of masonry research results.

The main danger in this lack of knowledge lies in the response of masonry structures to seismic loading. Enough information has been accumulated through analysis and simple experiments to design structures that are quite safe under static conditions. But dynamic loading can produce markedly different stresses, including tensile stresses. While masonry is generally very strong in compression, most types are rather brittle, and can withstand much less tensile stress.

A result of this brittle behavior has been substantial damage to many masonry structures in areas that have experienced strong earthquakes [1]. But in the same area where some masonry structures have been destroyed, others have survived undamaged. It appears, therefore, that through analysis and a knowledge of material behavior, it should be possible to reduce the seismic hazard.

In an effort to provide this knowledge and necessary analysis techniques, an extensive research program, sponsored by the National Science Foundation, was undertaken at the University of California, San Diego. The program consists of experimental, analytical, and numerical investigations of the behavior of masonry material and connections. For further information about this program see references [2] through [8]. The subject of this dissertation is an analytical representation of selected experimental results on material behavior.

CHAPTER 1. OBJECTIVES AND METHODOLOGY

1.1 Scope of Study

In conducting an investigation into the behavior of a material as complex and variable as masonry, it is necessary to limit the scope of the study. Some of the material variables to be considered are block type, mortar type and amount, grout type and amount, method of compaction, and amount of reinforcing. (These terms are illustrated in Fig. 1.1.) Instead of looking at the effects of these variables, attention was restricted to a few combinations, which were selected on the basis of their widespread use in construction. The intent of this restriction was to allow a thorough study of the masonry types selected.

The results presented in this dissertation are further restricted. They are based on tests of a single combination of components, and all specimens were fully grouted. While partially grouted masonry is widely used and deserves study, fully grouted masonry is of importance in seismically active areas, and such specimens are easier to handle because of their greater strength. Both unreinforced and reinforced masonry are discussed.

In addition to selecting a material type, it is necessary to decide what properties will be investigated. In the UCSD program, only in-plane loads were considered. Though damaged structures sometimes exhibit out-of-plane failures, walls that suffer such displacements probably do so only after substantial damage has occurred.

Thus, knowledge of planar behavior should enable one to predict the response of a structure until it is close to collapse.

1.2 Method of Investigation

In studying this planar behavior, two approaches are possible. One is to test structural elements, for example piers, then to combine these results to predict the behavior of a structure. Such a program exists at the University of California, Berkeley [9]. But the number of possible elements and their variations can necessitate a large number of tests. The other approach, employed in this program, is that of continuum mechanics. If one can determine the properties of the material, then through analysis one can predict the behavior of the structural elements, and a complete structure. The structural element tests can serve as an important check on this process.

The design of masonry buildings is presently based primarily on the uniaxial compressive strength, which is determined by prism tests (see Section 3.1). Other tests that have been conducted include beam tests and diagonal compression tests. These other tests cannot, however, determine a material behavior law relating stress to strain. While the state of stress for such loading may be known for an isotropic linear material, the solution does not hold for masonry, so the stress and strain are unknown.

In order to find such a law, one must be able to apply an arbitrary state of uniform planar stress. Such a stress state consists of two direct stresses, plus a shear stress. Direct stresses are fairly easy to apply, but the application of shear stress is quite difficult. To circumvent this difficulty, the following result of tensor analysis was taken advantage of: A general state of planar stress is equivalent to two direct stresses (the principal stresses) with zero shear stress, at some angle relative to the coordinate system of the original stresses [10]. This result is expressed quantitatively by Mohr's circle.

Since these direct stresses are to be applied to the edges of the specimen, the edges must be aligned with the principal stress directions. Thus, the masonry joints will, in general, not be aligned with the edges. Once a stress state is selected, the principal directions, and hence the specimen orientation, are determined. A disadvantage of this procedure is that for a particular specimen, the directions of the principal stresses are fixed.

The requirement that the stress be uniform applies, of course, only macroscopically. Treating a material as a continuum requires that variations in stress at the microscale be averaged out over several micro-dimensions. For masonry the micro-dimension is a block length, 16 inches. For this program, therefore, the size of the square specimen was chosen to be 64 inches.

1.3 Specimen Construction

The first step in producing these oblique lay-up specimens was the construction of 8-foot square walls, which were built by professional masons using conventional field practice. Grout was poured in 8-foot lifts and compacted by puddling. The materials used in construction are described in Table 1.1. After curing, a wall was faced on one side with a layer of hydrocal, then placed horizontally on the hydrocal. A dynamically balanced, high speed circular saw then cut out the specimen.

Reinforced specimens had two number five bars in each direction, for a steel to total area ratio of 0.13 percent, which is typical of masonry construction. These bars were carefully positioned to end just short of the specimen edge. After the specimen was cut, the grout was chipped away from the end of the bar, and a steel plate was welded to the bar and bonded in place with epoxy.

The walls for this program were fabricated in eight batches. Though materials and construction were the same for all batches, significant variations in strength between batches were observed. One batch that cured during a particularly wet period was considerably stronger than the others. Thus, when calculating average properties, it is necessary to restrict attention to a single batch.

1.4 Test Procedures

For the purpose of testing these specimens, a test frame capable of applying arbitrary biaxial stress was constructed. This frame, shown in Fig. 1.2, was designed to withstand the enormous loads required to fail a specimen, with only small deflections. The frame deflection must be small in order to control displacements when loads drop suddently at first fracture. A smaller frame was built for testing uniaxial specimens.

The biaxial frame actually consists of two parallel frames, between which are attached hydraulic actuators that deliver the load. The actuators are arranged four to a side, can deliver up to 120, 000 lbs each in either direction, and are controlled by a mini-computer. They are attached to 6-inch thick aluminum load distribution fixtures, which are bonded to the specimen (Fig. 1.3).

Two bonding materials were used. For unreinforced specimens the load fixtures were attached with a 0.25 inch layer of a polysulfide material having a low (~ 150 psi) shear modulus. This low shear modulus permitted large strains in the tensile direction with little drag. There was some concern that under compression the polysulfide might tend to extrude and thus cause tensile failure at the specimen edge, but tests at the highest level of compression showed no evidence of such an effect. In early tests the crack sometimes occurred near an edge, so a layer of epoxy 8 inches wide was added to both faces of each tensile edge, in order to force the crack into the center of the specimen (Fig. 1.3).

The bonding of reinforced specimens was comewhat more complicated. In order to transfer load to the steel, a steel plate was welded to each bar on the tensile edge, then epoxy bonded in place. The entire tensile edge was then bonded with epoxy to another steel plate, which was attached to the load distribution fixture. This procedure ensured that the steel would not debond from the much softer masonry. A polysulfide bond was again used on the compression side, in order to minimize shear drag.

In applying loads to the specimen, one tensile side was fixed in translation, and the other displaced at a prescribed rate. Both tensile sides were free to rotate. As the tensile load was applied, it was multiplied by a factor and applied to one of the compressive sides (proportional loading), which was also free to rotate. The opposite compressive side was actively prevented from either displacing or rotating. Thus, overall displacement and rotation were prevented, and uniform stress along each side was ensured.

Prism tests were also conducted as part of this investigation [11]. These tests were performed with a 300 kip Riehle machine under displacement control, and a ball and socket joint was used between the prism and the load platen in order to eliminate moments. The results were quite sensitive to prism end conditions, and these effects are discussed in Section 3.1.

1.5 Data Recording and Reduction

Data taken during biaxial tests consisted of the load applied by each hydraulic actuator, plus a number of displacements. The loads were measured by load cells placed in line with the actuators. The displacements were taken across the specimen at several locations, and were measured by linear variable differential transformers

(LVDTs). There were eight LVDTs available. They were usually arranged with two on each face parallel with the direction of tensile loading, three in the compressive direction, and one at a 45° orientation. This arrangement constitutes a strain rosette that defines the state of strain. The rods that the LVDTs were attached to can be seen in Fig. 1.3.

The signals from these instruments were processed by a high-speed digital data acquisition system, which recorded 300 samples/sec from each channel on magnetic tape. The information on tape was converted to plots by a computer program that allowed several channels to be combined and plotted versus either time or another combination of channels.

1.6 Data Selection

The number of large-scale specimens tested in this investigation was 94. Data from only about 40 specimens, however, are used in this dissertation. Reasons that data are excluded include bond failures, poor load distribution, incomplete displacement records, malfunction of recording equipment, the necessity of comparing results only within a batch, and the commitment of one batch to a study of grout admixture and vibration.

For the elasticity results of Chapter 2, only two specimens that had a complete strain rosette were tested at the orientation required for accurate analysis. For the uniaxial tensile strength results of Section 3.2, only two batches had a sufficient number of uniaxial specimens to permit the determination of a curve. The same requirement of a sufficient number of specimens within a batch limited the analysis of biaxial data to that from one batch. Finally, difficulties with recording equipment, and some unfortunate crack patterns reduced the number of suitable reinforced specimens from eight to three.

Much of the data not used in this analysis was valuable, however, is discovering patterns of behavior and deciding what tests to conduct.

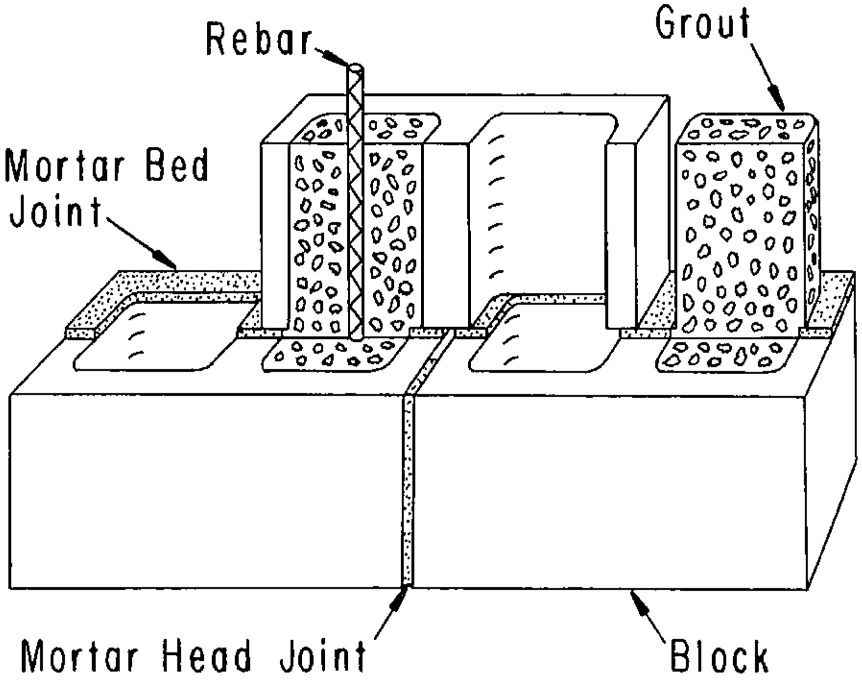

Fig. 1.1. Illustration of Masonry Terms

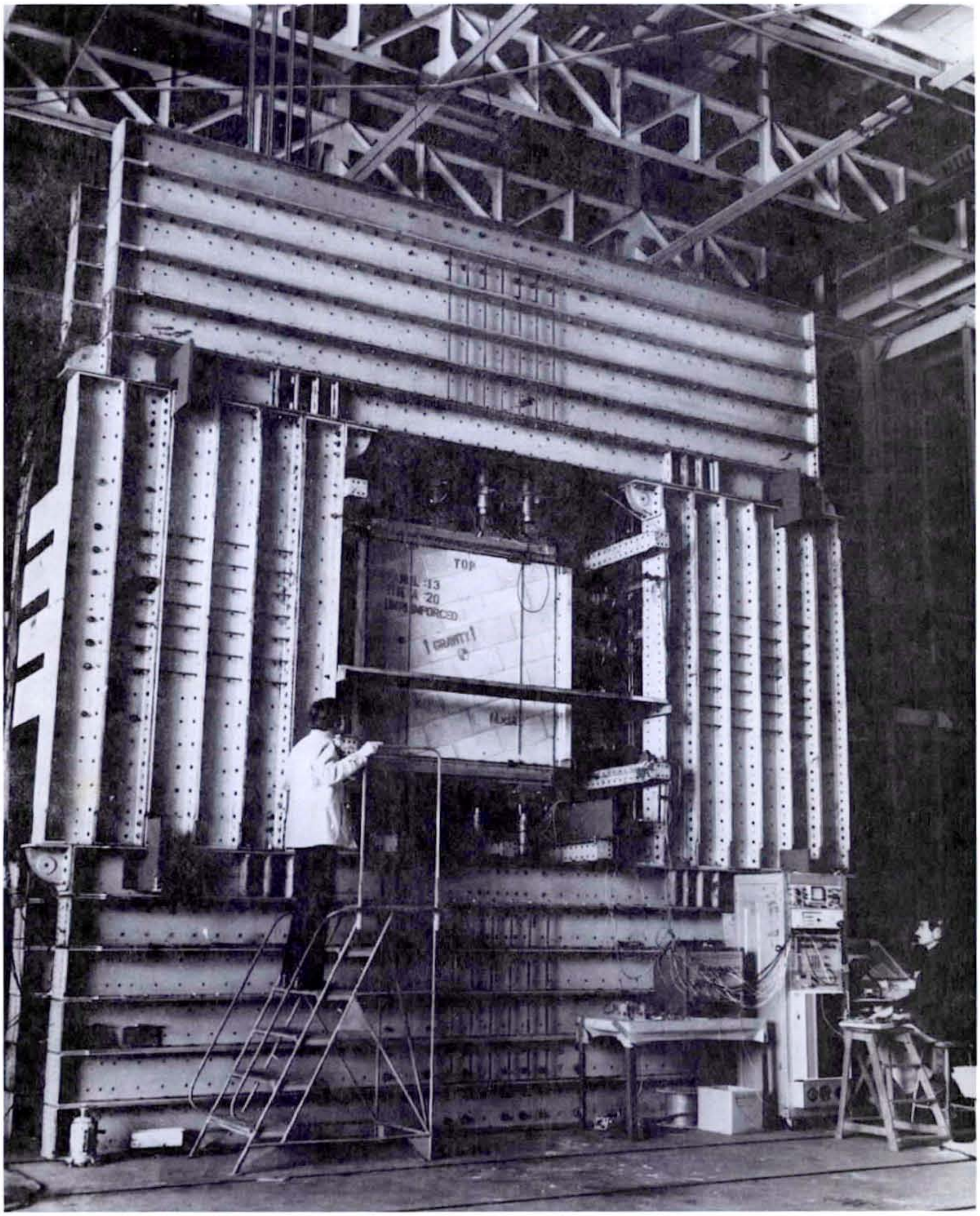

Fig. 1.2. Biaxial Test Frame

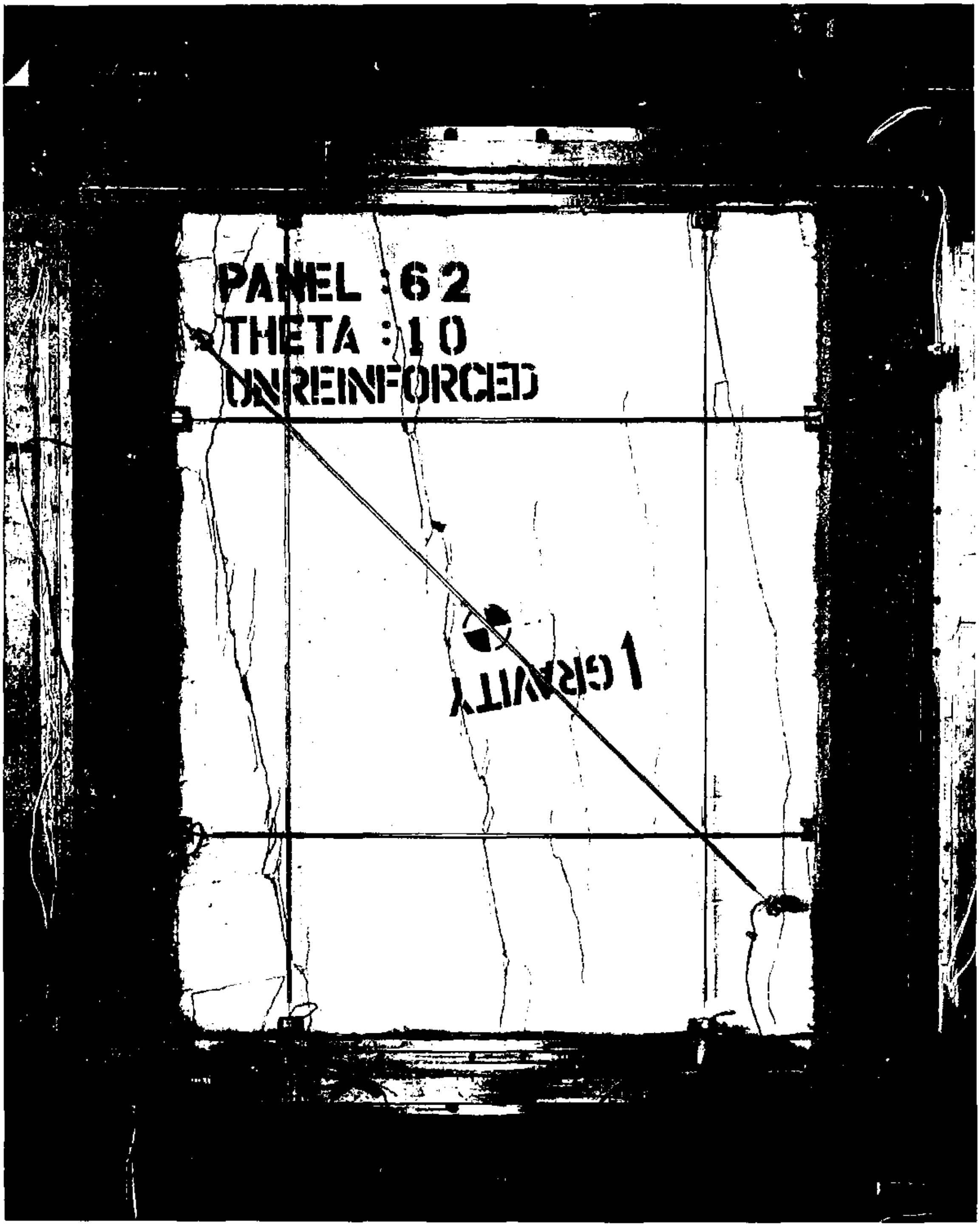

Fig. 1.3. Load Distribution Fixtures Bonded to Specimen

Table 1.1. Component Descriptions

	Block	Mortar	Grout
Description	Type N Normal weight ASTM C90	Type S ASTM C270	2000 psi coarse ASTM C476 (6-sack grout)
Compressive strength*	3300 psi	2420 psi	3870 psi
Tensile strength*	329 psi	215 psi	266 psi
Young's modulus	2.5×10^6 psi	-	2.6×10^6 psi

Reinforced specimens with #5 (grade 60) rebar.

---

* Strengths from 4 in. × 6.5 in. block coupons, and grout and mortar cylinders.

CHAPTER 2. ELASTIC BEHAVIOR

The first step in the analysis of a structure is to determine its elastic response. Even if one's interest is in the response once fracture has begun, prediction of the commencement of fracture requires knowledge of the behavior in the elastic range. For masonry, this behavior is quite simple for loadings usually encountered. Except, perhaps, in the high compressive stress range, masonry has a very linear response up until first cracking. This linear behavior is defined by the elastic moduli. One also needs to know the material damping for a complete description of the elastic behavior. If it is large enough, material damping can be of importance in energy dissipation.

2.1 Form of Elastic Law

In this treatment of the behavior of masonry, out of plane loading is assumed zero. If a coordinate system is aligned with the joint directions as shown in Fig. 2.1, the stresses and strains of interest are $(\sigma_{11}, \sigma_{22}, \sigma_{12}, \sigma_{21})$ and $(e_{11}, e_{22}, e_{12}, e_{21})$. Either set is assumed to determine the other.

This geometry and loading is one that is frequently encountered, of course. From the behavior of the material at each point in the thickness direction, the overall behavior is commonly derived by assuming a plane stress condition, then integrating stresses across the thickness. If masonry is considered solid, such a procedure is valid. But grout cores adhere poorly to the cell walls, and there are voids in the grout and at the head joints. For partially grouted masonry, in fact, a stress-strain relation at a point in the thickness direction cannot be defined, for such an element fails to be a continuum. Therefore, elastic behavior will be analyzed without considering the variation in stress through the thickness.

Since this analysis will disregard the thickness direction, it would be more correct to discuss stress resultants (force per unit length) rather than stress. But since strength is commonly expressed in terms of stress, this is not done.

Plots of the above stresses versus strain are very linear almost until fracture. Therefore, assume that within some range the following linearity condition holds:

$$\sigma_{ij} = C_{ijk\ell}\, e_{k\ell} \quad ,$$

where the subscripts have the range (1, 2), and repeated subscripts indicate summation.

If one assumes the existence of a strain energy function W such that

$$\sigma_{ij} = \frac{\partial W}{\partial e_{ij}} \quad ,$$

then one has symmetry of the above matrix: $C_{ijk\ell} = C_{k\ell ij}$. Such a function exists for the three-dimensional case, and the proof of its existence [12] holds for this case of stress resultants, at least for static situations.

If the above matrix is inverted, one has the symmetric matrix $c_{ijk\ell}$ such that

$$e_{ij} = c_{ijk\ell}\,\sigma_{k\ell} \quad .$$

Because of symmetry of the stress tensor ($\sigma_{12} = \sigma_{21}$), terms can be combined to give the form

$$\begin{bmatrix} e_{11} \\ e_{22} \\ e_{12} \end{bmatrix} = \begin{bmatrix} c_{1111} & c_{1122} & c'_{1112} \\ c_{1122} & c_{2222} & c'_{2212} \\ c_{1211} & c_{1222} & c'_{1212} \end{bmatrix} \begin{bmatrix} \sigma_{11} \\ \sigma_{22} \\ \sigma_{12} \end{bmatrix} \quad ,$$

where the symmetry condition $c_{1122} = c_{2211}$ has been employed, and the equation for e_{21} ($= e_{12}$) has been eliminated.

There is one further condition that can be used to simplify the above relation. That condition is material symmetry. If the x_1 axis is reversed in sense, the form of the above law cannot be affected, for the x_2 axis is a line of symmetry. (Note that this would not be the case for a wall constructed of block open at one end and closed at the other.) Reversing the sense of the x_1 axis will change the signs of e_{12} and σ_{12}, while leaving the other stresses and strains unchanged. Hence, one concludes

$$c'_{1112} = c'_{2212} = c_{1211} = c_{1222} = 0 \; .$$

With new names for the four constants, the relation becomes

$$\begin{bmatrix} e_{11} \\ e_{22} \\ e_{12} \end{bmatrix} = \begin{bmatrix} 1/E_1 & -2\nu/(E_1+E_2) & 0 \\ -2\nu/(E_1+E_2) & 1/E_2 & 0 \\ 0 & 0 & 1/2G \end{bmatrix} \begin{bmatrix} \sigma_{11} \\ \sigma_{22} \\ \sigma_{12} \end{bmatrix} . \quad (2.1)$$

2.2 Determination of Elastic Moduli

Direct determination of the values of the four elastic moduli is possible by applying loads in the following manner: First set $\sigma_{22} = 0$, while σ_{11} is non-zero. This will determine E_1. Switching roles for the two stresses then determines E_2 and ν. Any stress state having $\sigma_{12} \neq 0$ will determine G.

In this investigation, specimens were tested by applying direct (zero shear) loads to edges cut at a lay-up angle θ. With the coordinate systems shown in Fig. 2.2, this implies that $\sigma'_{12} = 0$. Under this restriction, stresses transform as follows:

$$\begin{aligned} \sigma_{11} &= \sigma'_{11} \cos^2\theta + \sigma'_{22} \sin^2\theta \\ \sigma_{22} &= \sigma'_{11} \sin^2\theta + \sigma'_{22} \cos^2\theta \\ \sigma_{12} &= (-\sigma'_{11} + \sigma'_{22}) \cos\theta \sin\theta \end{aligned} \quad (2.2)$$

Two orientations have special significance in these relations. For $\theta = 45°$, one has $\sigma_{11} = \sigma_{22}$ for all values of σ'_{11} and σ'_{22}. Because of this, the three moduli E_1, E_2, and ν cannot be determined for a 45° specimen. Clearly, for values of θ near 45°, their determination will be difficult. For $\theta = 0°$, on the other hand, one has $\sigma_{12} = 0$, so that G cannot be determined. Hence, an intermediate value of θ is necessary in order to determine all four moduli accurately. For this reason, specimens having a lay-up angle $\theta = 20°$ were chosen for the determination of elastic moduli.

From the above equations, one finds that, for direct determination of the moduli, the applied loads must satisfy these conditions:

$$\sigma'_{22} = -\sigma'_{11} \tan^2\theta \qquad (\Rightarrow \ \sigma_{22} = 0)$$

$$\sigma'_{11} = -\sigma'_{22} \tan^2\theta \qquad (\Rightarrow \ \sigma_{11} = 0)$$

Note that each of these relations necessitates a tensile load. Because of the low tensile strength of masonry, care must be taken in conducting such a test not to fail the specimen prematurely. In the tests we performed, the second condition was satisfied during a test in which a failure strength of the specimen was determined. However, no test was conducted that satisfied the first condition. Hence, determination of the moduli was somewhat more complicated than in the procedure described above.

The tests that were conducted (for most specimens) were the following three: horizontal compression ($\sigma'_{22} = 0$), vertical compression ($\sigma'_{11} = 0$), and a failure test with $\sigma_{11} = 0$. From the failure test one can find E_2 and the term $-2\nu/(E_1 + E_2)$. Then one can determine E_1 from the horizontal compression test. This requires the value of $-2\nu/(E_1 + E_2)$, but since it multiplies the small quantity

σ_{22}, an error in its value will have a small effect. Finally, any one of the three tests is suitable for determining G.

2.3 Analysis of Moduli Data

The data taken during the tests included the loads applied to the edges of the specimens, and displacements in three directions across the specimens. These are shown in Fig. 2.3. The loads were applied as shown for all specimens, but the configuration of the displacement gauges varied somewhat.

The edges of the specimen correspond to the x_1' and x_2' directions (see Fig. 2.2). Hence, the stresses are given by

$$\sigma'_{11} = (LD13 + LD14 + LD15 + LD16)/488 \text{ in}^2$$

$$\sigma'_{22} = (LD1 + LD2 + LD3 + LD4)/488 \text{ in}^2$$

$$\sigma'_{12} = 0$$

In the horizontal direction, the loads on each side of the specimen agreed very closely. In the vertical direction, gravity produced a difference of several psi between the loads at the top and the loads at the bottom of the specimen. For determination of elastic moduli, this offset is of no significance.

While the actual stresses were known, only changes in strains were available, because the LVDTs were not set to read zero at zero load. To find the change in strain, each displacement was divided by its gauge length, then the resulting strains were averaged. For the configuration of Fig. 2.3 this gives

$$\Delta e_{11} = \Delta \left(\frac{D1H}{GL1H} + \frac{D2H}{GL2H} + \frac{D3H}{GL3H} + \frac{D4H}{GL4H}\right)\Big/4$$

$$\Delta e'_{22} = \Delta \left(2\frac{D1V}{GL1V} + \frac{D2V}{GL2V} + \frac{D3V}{GL3V}\right)\Big/4$$

$$\Delta e_D = \Delta \frac{D1D}{GLD}$$

Examination of displacements from many specimens showed little variation in readings from the same face of the panel (e.g. D1V and D2V), but frequent significant variation, as much as 20 percent, from front to back. This is the reason that D1V is multiplied by 2. For the same reason, e_D may suffer some error, since only one LVDT was available for its measurement.

The first step in analysis of the data was to determine a set of stresses and corresponding strains. These strains were found from plots of stress versus strain. For uniaxial loading, all three strains were plotted versus the applied load. For the failure test, both stresses were used, and corresponding values of the two stresses were found from plots of stress versus time.

An example of a stress-strain plot for several cycles of compression is shown in Fig. 2.4. Because the specimen was preloaded, the stress does not go to zero. To find the strain corresponding to a stress, a straight line was extrapolated to the zero-stress level along the path of increasing load, as shown by the broken line.

From the specimens tested in this investigation, two were selected that were best suited for elastic moduli determination. For many of the early specimens, determination of all four moduli was impossible, because only horizontal and vertical strains were measured. Of the remaining specimens, there were two tested at the desired 20° lay-up angle. These two specimens, nos. 79 and 84, were from the same batch, so their properties should be very similar.

The strains measured for these two specimens are given in Table 2.1. These three extensional strains (e'_{11}, e'_{22}, e_D) constitute a strain rosette, (0°, 90°, 45°), and from them the shear strain e'_{12} can be determined. The transformation of strain components is given by

$$\begin{aligned} e_{11} &= e'_{11} \cos^2\theta + e'_{22} \sin^2\theta + 2e'_{12} \cos\theta \sin\theta \\ e_{22} &= e'_{11} \sin^2\theta + e'_{22} \cos^2\theta - 2e'_{12} \cos\theta \sin\theta \\ e_{12} &= (-e'_{11} + e'_{22}) \cos\theta \sin\theta + e'_{12}(\cos^2\theta - \sin^2\theta) \end{aligned} \qquad (2.3)$$

The strain e_D, which is measured by the LVDT labeled D1D in Fig. 2.3, is seen to be the strain e_{22} for $\theta = 45°$. Therefore, one has

$$e_D = \frac{e'_{11} + e'_{22}}{2} - e'_{12} \, , \qquad (2.4)$$

whence

$$e'_{12} = \frac{e'_{11} + e'_{22}}{2} - e_D \, . \qquad (2.5)$$

Once the shear strain e'_{12} has been determined from Eq. (2.5), Eqs. (2.3) yield the strain components in the (unprimed) lay-up coordinate system. Equations (2.2) serve to transform stress components. By applying these transformations to the stresses and strains of Table 2.1, one obtains the results listed in Table 2.2.

One can now employ the procedure described in Section 2.2 to determine the elastic moduli. Though the stress σ_{11} is not zero, as assumed in Section 2.2, it is small enough to be neglected in order to obtain a first estimate of the values of the moduli. With those estimates one can then correct for the non-zero value of σ_{11}. The results are given in Table 2.3, where G is taken to be the average from the three tests.

With the values of the moduli known, it is now possible to predict, from the applied loads, the strains measured in the experiments. One first transforms the stress components from the primed system to the unprimed system by use of Eqs. (2.2), then finds the lay-up coordinate strains from Eqs. (2.1), then transforms to the primed coordinate strains using

$$\begin{aligned} e'_{11} &= e_{11} \cos^2\theta + e_{22} \sin^2\theta + 2e_{12} \cos\theta \sin\theta \\ e'_{22} &= e_{11} \sin^2\theta + e_{22} \cos^2\theta - 2e_{12} \cos\theta \sin\theta \\ e'_{12} &= (-e_{11} + e_{22}) \cos\theta \sin\theta + e_{12}(\cos^2\theta - \sin^2\theta) \end{aligned} \tag{2.6}$$

The final step is to find e_D from Eq. (2.4).

The values of the moduli given in Table 2.3 were determined by using only part of the data available from the experiments. The predicted values of the remaining data will, of course, suffer some error. In order to minimize these errors, it is necessary to use all of the data in the moduli calculations.

To do this, the predicted values for the three measured strains were computed, then the moduli values were refined so as to reduce the largest errors. By calculating the coefficients of each modulus in the expressions for the strains e'_{11}, e'_{22}, e_D, it becomes evident how to alter the moduli. The greatest change was in the value of ν. One might expect ν to be difficult to determine, since its value requires the measurement of a rather small strain. The refined values are given in Table 2.4.

Two items are noteworthy in these results. One is the small value of ν compared to its value for metals. The other is the strong anisotropy: This material is twice as stiff in the vertical direction as in the horizontal direction. This difference in stiffness may be partly due to the head joints. There is little mortar between adjacent blocks in the same course, so this joint will probably suffer substantial deformation. In contrast, the grout cores run uninterrupted in the vertical direction, and the bed joints are more completely mortared and have the benefit of compression due to gravity during curing.

Another reason may be that the grout contributes little to stiffness in the horizontal direction. Examination of the cut edges of specimens shows frequent separation of cores from the block. This separation could mean that the grout is not being loaded during horizontal compression.

The values of the strains predicted using the moduli values listed in Table 2.4 are given in Table 2.5. The measured strains are given in Table 2.1, and the predicted values follow from the measured loads (Table 2.1), and the transformation laws given above. One can see that most predicted values are within 20 percent of the measured values, and the worst percentage errors occur for the strains of small magnitude.

The error in these results probably is due principally to uncertainty in measurement of displacements. From the plots of stress versus strain (e.g. Fig. 2.4), the uncertainty in the strains used in these calculations can be estimated, and from this follows the uncertainty in moduli, listed in Table 2.6.

2.4 Material Damping

A structure subjected to dynamic loading must have some means of dissipating the energy it acquires, so that displacement amplitudes can be limited. Two mechanisms for losing energy are radiation into the ground, and frictional losses at the joints between structural members. A third mechanism is internal damping of the structural material. If the material from which the structure is built has a high level of damping, this third mechanism can be an important means of energy dissipation.

In this investigation the large-scale specimens were subjected to cyclic uniaxial compressive loading at several frequencies ranging from 0.05 cps to 2 cps. The nature of the hysteresis loops observed in these tests determines how the material damping should be modeled. If the damping is to be considered viscous, then the energy loss per cycle must be proportional to frequency. But no such frequency dependence was observed. As Fig. 2.5 shows, there is no measurable change in energy loss over a range of frequencies of nearly two orders of magnitude.

This frequency independence is a characteristic of hysteresis damping [13], also called solid or structural damping. The damping is due to friction between internal planes which slide during deformation, and this type of damping is exhibited by many materials, for example rubber and steel. The energy loss per cycle for hysteresis damping is proportional to the square of the displacement amplitude, which means that the hysteresis loops have the same shape for all displacement amplitudes.

All specimens tested in this investigation were subjected to cyclic loading at approximately the frequencies shown in Fig. 2.5, and these curves are typical. Only one specimen, however, was tested over a range of displacement amplitudes. Its damping results are given in Table 2.7, and they are seen to satisfy closely the amplitude dependence assumed for hysteresis damping.

This specimen was loaded to about half its failure load in compression. At this level, a small increase in energy loss was observed, and it is likely that significant increases will occur for loads approaching the compressive failure load. At the stress levels applied to the remaining specimens, the areas of the hysteresis loops are quite small, which makes their measurement difficult. Table 2.8 gives the areas at several orientations. If there was any dependence on angle or batch, it was too small to be detected.

As noted above, the energy loss per cycle for hysteresis damping is proportional to the square of the amplitude. It is clear that a member with a larger cross-sectional area will have a larger energy loss for the same displacement. If one includes the stiffness of the member in the proportionality relation, the shape of the member will then be accounted for, and the remaining proportionality factor will be a dimensionless hysteresis damping constant for the material. Thus, the energy loss per cycle is

$$\Delta U = \pi k b D^2 \quad ,$$

where k is the stiffness, D is the displacement amplitude, and b is the damping constant. The factor π is included in order to simplify a later result. For our specimens it was found that $b \cong 0.040$.

Some understanding of the effect this type of damping will have on the motion of a structure can be obtained by a simple analysis. Imagine a material element which exhibits small hysteresis damping acting as a massless spring in a system undergoing free vibration about the equilibrium point X (Fig. 2.6). The resulting motion will be harmonic with slowly decaying amplitude. This would be just the loading that a structural member of a building undergoing free vibration in its first mode would experience. The energy loss for the building would be the sum of the energy losses of the members.

Let the material element have the force-displacement curve for cyclic loading shown in Fig. 2.7, where X is the displacement due to the constant load kX, and D is the cyclic displacement amplitude. The force g represents the deviation from linearity, so that the total force is $f = kx + g$, and the energy loss per cycle is

$$\Delta U = \oint g \, dx \quad .$$

The equation of motion for the mass is

$$kX - (kx + g) = m\ddot{x} \quad .$$

By multiplying this equation by x and integrating over time, one finds the energy equation

$$kX \, \Delta x - \frac{1}{2} k \, \Delta(x^2) - \int g \, dx = \frac{1}{2} m \, \Delta(\dot{x}^2) \quad .$$

Applying this equation at the beginning and end of a cycle, where $\dot{x} = 0$, gives

$$kX(D_2 - D_1) - \frac{1}{2} k \left[(X + D_2)^2 - (X + D_1)^2 \right] - k\pi b \, D_1^2 = 0 \quad ,$$

where the above expressions for ΔU have been used. Solving for D_2, one finds

$$D_2 = \sqrt{1 - 2\pi b}\, D_1 \quad ,$$

or,

$$D_2/D_1 \cong 1 - \pi b \quad .$$

Thus, the ratio of successive amplitudes is constant, which means the decay is exponential. If one knows this ratio for a vibrating structure, he can then find the damping constant b. (As noted above, though, there are other sources of damping for a structure, which would add to the damping due to b.)

Since the decay due to viscous damping is also exponential, the free-vibration behavior of the system analyzed above is identical to that of a certain viscous damped system with spring and damper in parallel. For a viscous damped system, the damping rate is characterized by the damping factor ξ, equal to the ratio of the damping constant to the critical damping constant. (ξ times 100 is the percent critical damping.) For small ξ, the ratio of successive amplitudes is

$$D_2/D_1 \cong e^{-2\pi\xi} \quad .$$

Using the above result, one finds

$$\xi \cong b/2 \quad .$$

Hence, one can say that the material is characterized by a damping factor equal to half of b, and our specimens exhibited a 2.0 percent critical damping.

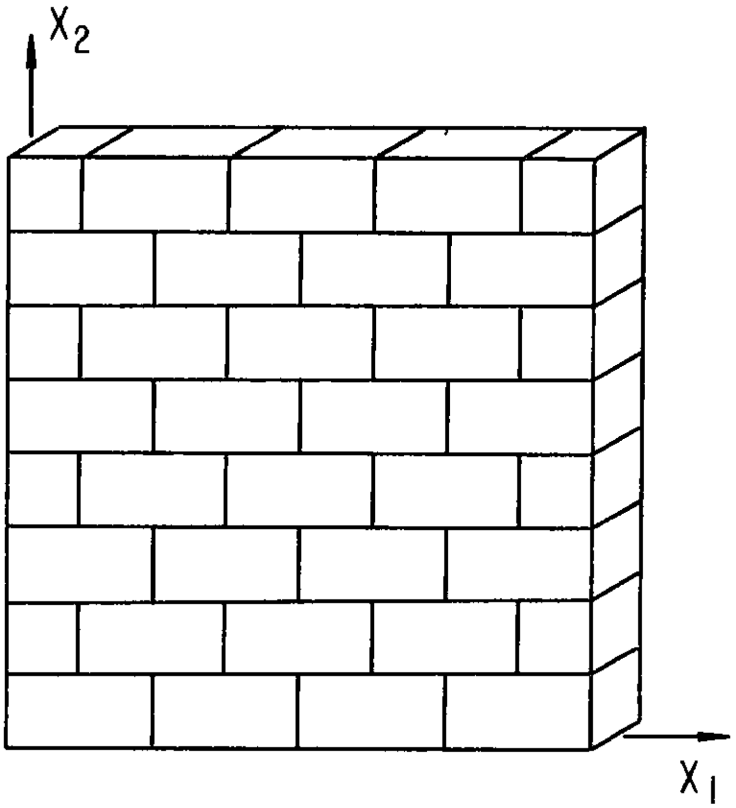

Fig. 2.1. Joint Coordinate System

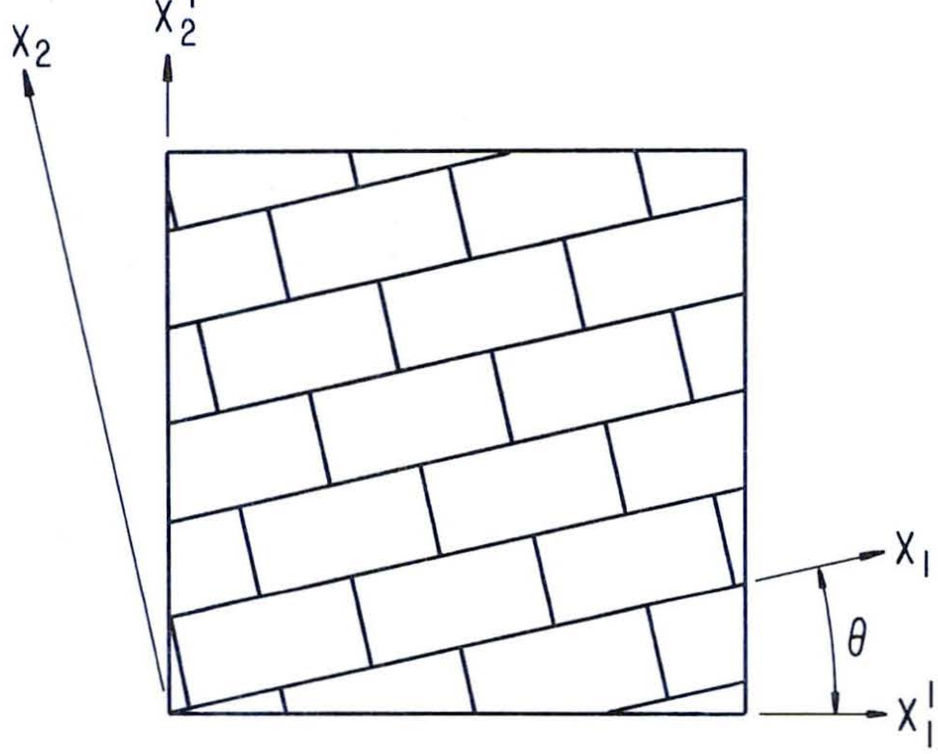

Fig. 2.2. Joint and Principal Stress Coordinate Systems

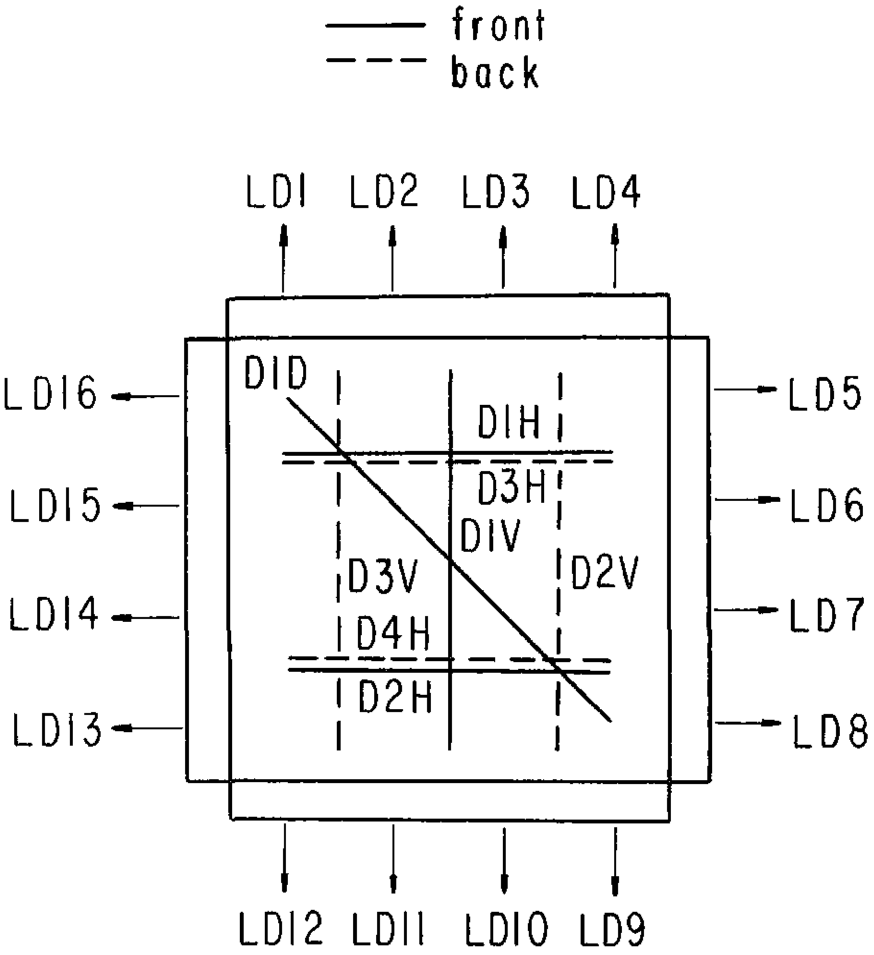

Fig. 2.3. Load and Displacement Names

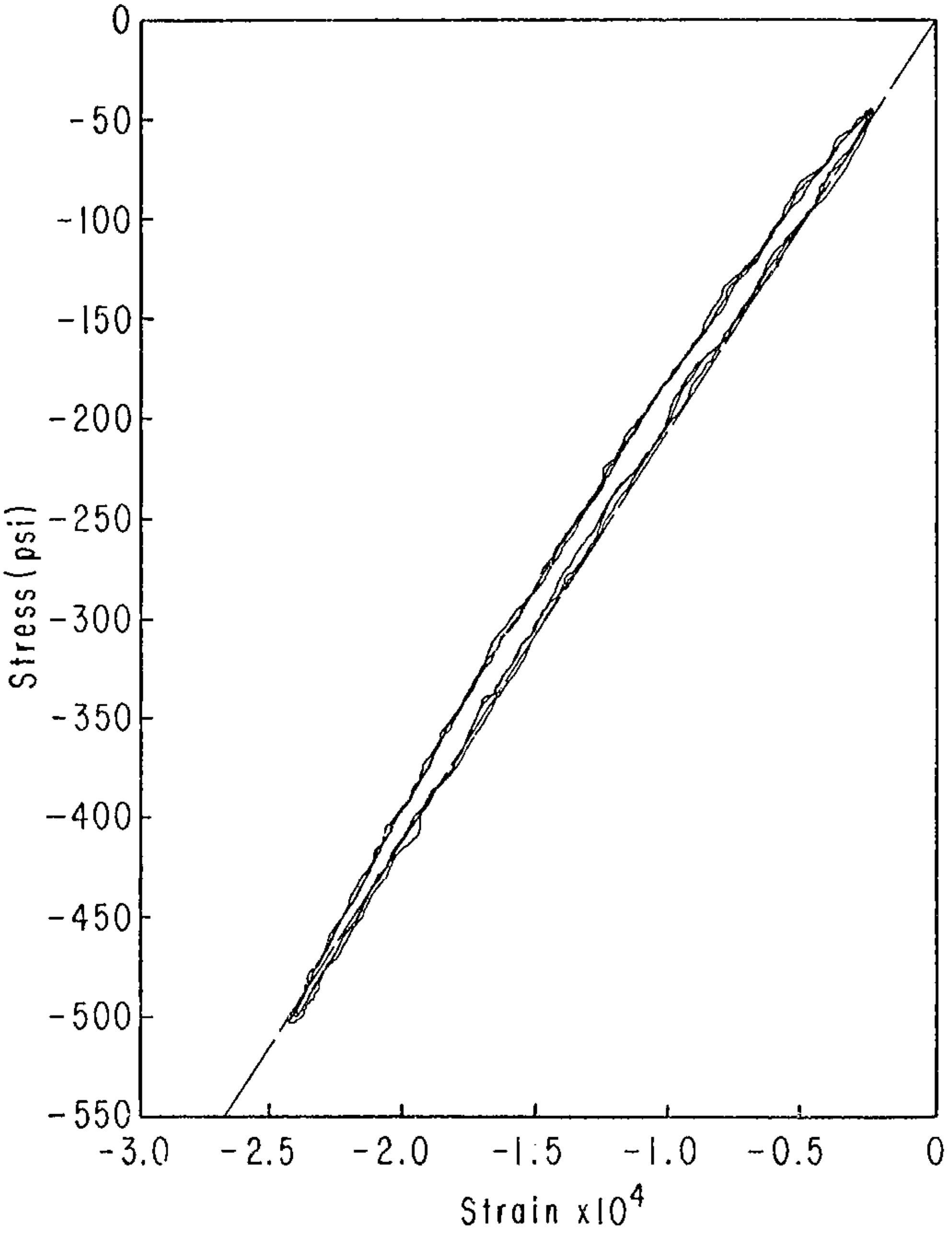

Fig. 2.4. Example of a Stress-Strain Plot

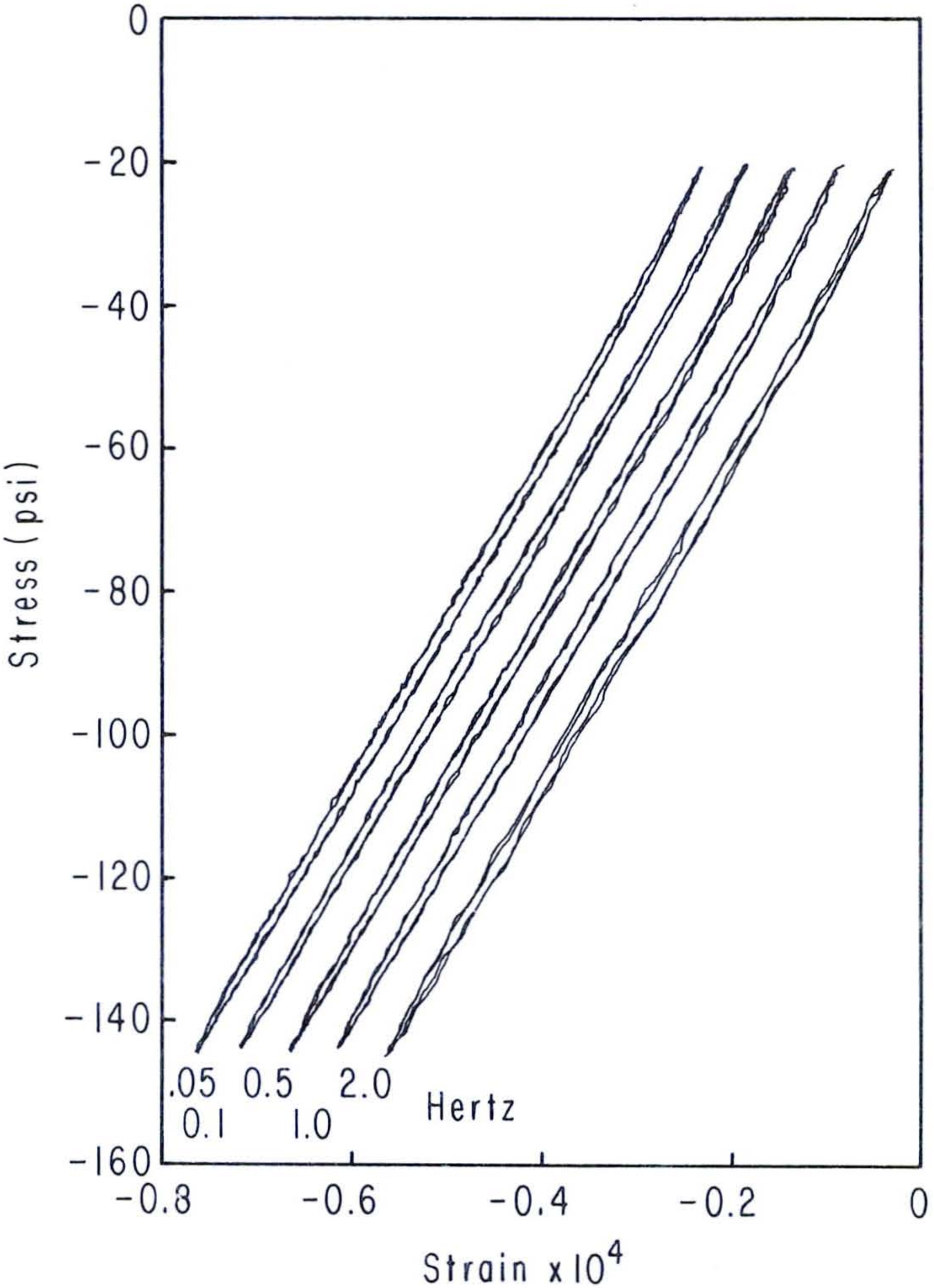

Fig. 2.5. Uniaxial Compression Hysteresis Loops

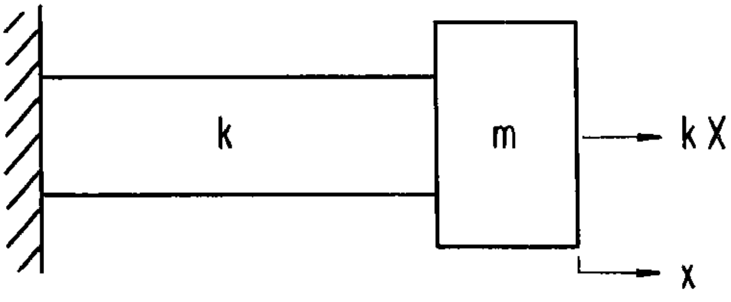

Fig. 2.6. Vibrating Spring-Mass System

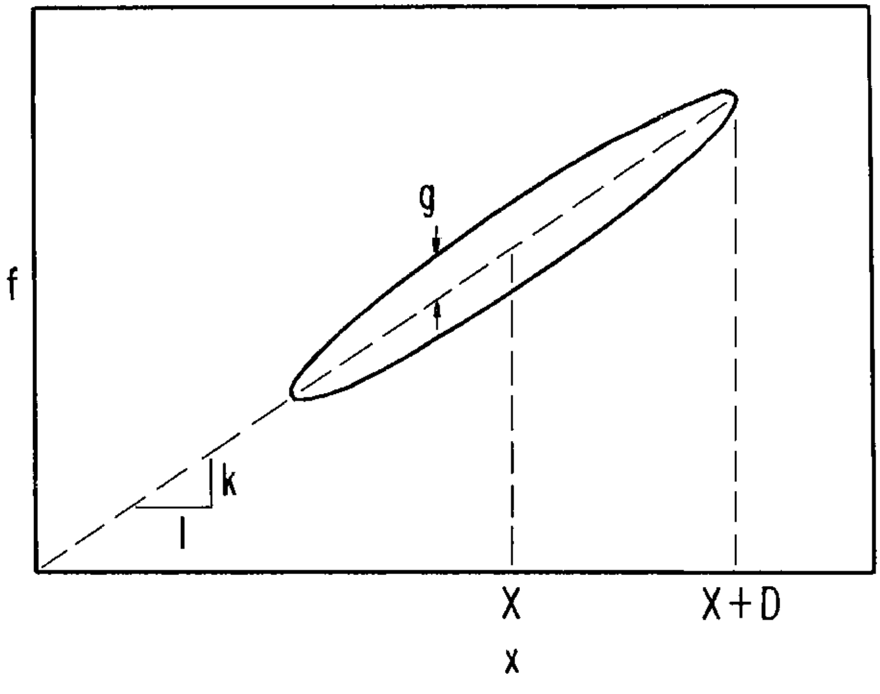

Fig. 2.7. Force-Displacement Curve of Hysteresis-Damping Spring

Table 2.1. Elastic Strains ($\times 10^6$) and Stresses (psi) in Principal Stress Coordinate System

Panel #	Test	e'_{11}	e'_{22}	e_D	σ'_{11}	σ'_{22}
79	Horizontal	-182	18.2	-63.1	-180	0
	Vertical	43.7	-196	-41.7	0	-350
	Failure	106	-180	-13.1	42.1	-300
84	Horizontal	-176	20.7	-62	-180	0
	Vertical	37.9	-207	-32.8	0	-350
	Failure	94.1	-184	-11.5	40.1	-300

Table 2.2. Elastic Strains ($\times 10^6$) and Stresses (psi) in Joint Coordinate System

Panel #	Test	e_{11}	e_{22}	e_{12}	σ_{11}	σ_{22}	σ_{12}
79	Horizontal	-171	6.8	50	-159	-21	58
	Vertical	-6.5	-146	-103	-41	-309	-112
	Failure	57	-131	-110	2.1	-260	-110
84	Horizontal	-163	7.7	51	-159	-21	58
	Vertical	-24	-145	-118	-41	-309	-112
	Failure	40	-130	-115	0.3	-260	-109

Table 2.3. Elastic Moduli, First Estimate

Panel #	E_1 (10^6 psi)	E_2 (10^6 psi)	G (10^6 psi)	ν
79	0.907	1.992	0.541	0.31
84	0.957	2.001	0.506	0.23

Table 2.4. Elastic Moduli, Final Estimate

Panel #	E_1 (10^6 psi)	E_2 (10^6 psi)	G (10^6 psi)	ν
79	0.912	2.041	0.526	0.19
84	0.957	2.037	0.488	0.16

Table 2. 5. Predicted Elastic Strains ($\times 10^6$)

Panel #	Test	e'_{11}	e'_{22}	e_D
79	Horizontal	-186	24.4	-64.4
	Vertical	47.5	-198	-39.2
	Failure	84	-176	-18.6
84	Horizontal	-182	25.3	-69
	Vertical	49.2	-205	-34.4
	Failure	82.6	-182	-14.0

Table 2. 6. Uncertainty in Moduli Values

Modulus	E_1 (10^6 psi)	E_2 (10^6 psi)	G (10^6 psi)	ν
Uncertainty	± 0.03	± 0.08	± 0.03	± 0.04

Table 2.7. Damping versus Displacement Amplitude

σ_{max} (psi)	Amplitude* (10^{-3} in.)	Loop Area (in. lb)	$\frac{\text{Area}}{k^{\dagger} \cdot \text{ampl.}^2}$
170	1.34	7.32	0.204
330	3.20	36.0	0.176
490	5.32	93.1	0.164
670	7.72	198	0.166
820	10.23	372	0.178

*(max-min)/2.

†k is the panel stiffness = 2.0×10^7 lb/in.

Table 2.8. Damping versus Lay-up Angle

Panel Number	Angle (degrees)	Freq. (Hz)	$\frac{\text{Area}}{\pi k \text{ ampl.}^2}$
32	30	0.5	.0429
32	-60	0.5	.0369
35	90	0.5	.0454
36	90	0.5	.0448
38	90	0.1	.0322
40	45	0.5	.0326
43	75	0.5	.0306
45	0	0.5	.0249
46	15	0.5	.0521
48	45	0.5	.0341
48	-45	0.5	.0503
50	0	0.05	.0204
51	30	0.5	.0303
53	30	0.5	.0418
79	20	0.1	.0378
84	20	0.1	.0356

CHAPTER 3. INITIAL STRENGTH

The strength of masonry is defined by a closed surface in stress space (σ_{11}, σ_{22}, σ_{12}) at which first cracking occurs. The tests conducted in this investigation do not determine the entire surface, but concentrate on a part of the surface that should be of greatest importance in the analysis of buildings subjected to seismic loading.

Both uniaxial and biaxial strength tests were conducted, and uniaxial specimens were tested both in compression and tension. The biaxial tests were restricted to the following special case: The principal stresses and their orientation were chosen to render the normal stress on the head joint planes zero. This restriction was made because it is believed that in structures this stress is usually small compared to the shear stress or the normal stress on the bed joint planes:

$$|\sigma_{11}| \ll \max(|\sigma_{22}|, |\sigma_{12}|)$$

3.1 Uniaxial Compressive Strength

Before looking at the general case of biaxial stress, consider the special case in which one of the principal stresses is zero and the other negative (compressive). For this case there remains one variable to be specified: the angle at which the stress acts relative to the bed-joint planes. Though the compressive strength and its dependence on lay-up angle should be determined by tests on large-scale panels, our test system did not have the ability to load to failure in compression. Hence, we were forced to determine compressive strength by tests on small-scale specimens, and we were unable to determine its direction dependence.

The direction of loading which is easiest to test is that direction in which masonry is normally loaded - with compression across the bed joints. The strength in that direction is related to the quantity f'_m, which plays a major role in the design of structures. Building codes employ f'_m to limit allowable stresses. Its value is determined by tests on prisms, which are small assemblages consisting of two or more blocks laid up in a column. Specifically, f'_m is determined by tests of two-course prisms capped with a high-strength sulphur fly-ash compound or a high-strength gypsum plaster [14]. f'_m is taken to be the failure load in compression divided by the cross-sectional area of the prism.

As part of this investigation we examined the significance of f'_m as determined by the above procedure [9]. We found that two factors significantly affect the results obtained. The first is end restraint. Friction between the specimen and the bearing plates of the testing apparatus greatly restricts lateral displacement at the ends of the specimen. This restraint results in a higher failure load than would be obtained if the restraint were absent.

Evidence of this restraint is found in the failure mode - in a two-course prism the fracture surface bends away from the bearing plate to leave a roughly conical piece attached to the bearing plate (Fig. 3.1) - and in the lower strengths obtained with prisms of more than two courses. For prisms of three courses, the end effects are smaller at the center of the prism, so that the stress state begins to approach one of true uniaxial compression. This results in proper tensile splitting in the center block (Fig. 3.2). The proper stress state is nearly achieved in prisms of four courses, so there is little variation in strength between four-course prisms and those of five courses.

This interpretation of the effects of prism height leads to the conclusion that a two-course prism should behave similarly to a four-course prism if friction between the specimen and the bearing plates were eliminated. One method of greatly reducing the friction is to use a soft capping material. We conducted tests of two-course prisms capped with a 0.25 inch thickness of a polymer material with a very low shear modulus (about 150 psi). The results were as anticipated. The failure stress was about equal to that of a four-course prism, and the failure mode was tensile splitting that extended all the way to the ends of the specimens (Fig. 3.3). That this failure stress was not less than that of a four-course prism is evidence that the polymer does not cause premature failure by extrusion.

The other factor affecting the significance of prism tests is bond configuration. The two-course prisms which are tested to determine f'_m have no head joints. Two full blocks are simply laid up in stack bond. To determine if head joints influence the strength results obtained, tests were conducted on three- and five-course running bond prisms constructed from full blocks and half blocks. It was found that these prisms are significantly weaker than stack bond prisms of the same height. The reduction in strength for five-course prisms was about 16 percent.

The above results show that the value of f'_m obtained from two-course prism tests is much higher than the true compressive strength of full-scale masonry. The strength of a two-course stack-bond prism with a hard cap is about 62 percent higher than that of a five-course running-bond prism, which should be close to the strength of full-scale masonry. (This does not mean that the building codes are incorrect. This artificially high strength apparently has been accounted for in the safety factors. The true full-scale masonry strength is simply never considered in building design.)

It is possible that the narrow width (one full block wide) of a running-bond prism leads to a slightly premature failure in the head joints, but the error should be small. This possibility should be investigated by testing larger specimens, for example a five-course running-bond prism two full blocks wide. For this program we did not have a machine capable of performing such a test, so our best estimate of the compressive strength of full-scale masonry is that of a five-course running-bond prism.

3.2 Uniaxial Tensile Strength

Next consider the case in which one principal stress is zero and the other positive (tensile). For this case we were able to load large-scale panels to failure, and hence able to determine direction dependence.

A series of tests of direction dependence was conducted for each of two batches of specimens. The results are shown in Fig. 3.4. The variable θ represents the angle between the tension direction and the normal to the bed joints, so that $\theta = 0$ represents tension across the bed joints, and $\theta = 90°$ tension across the head joints.

For each batch there is a clear maximum strength for θ about 40°, with the strength gradually diminishing away from 40°. Thus, a second degree polynomial should provide an excellent representation of the dependence of strength on θ. Further, the variation in strength with θ is remarkably similar for the two batches, with batch 6 simply shifted up from batch 5. Therefore, it appears that one should know the strength for arbitrary θ if the strength for $\theta = 0$ is known.

For each batch, the values of the three constants for a second-degree polynomial fit of the data were determined by a least squares procedure. The results are given in Table 3.1, where

$$\sigma_t = \sigma_t^{(0)} + a\theta + b\theta^2 , \quad \theta \text{ in degrees} .$$

Since a and b show little variation between batches, the following formula should be an excellent representation of uniaxial tensile strength:

$$\sigma_t = \sigma_t^{(0)} + 0.67\,\theta - 0.009\,\theta^2 , \qquad 0 \le \theta \le 90° \qquad (3.1)$$

3.3 Biaxial Strength

The strength of masonry under biaxial loading was studied for the special case of zero head-joint normal stress. The behavior of fully grouted masonry was expected to be similar to that of concrete, which has been carefully studied. For concrete under biaxial loading, the tensile stress at which fracture occurs decreases approximately linearly with increasing compressive stress (see Fig. 3.5, from [15]).

In this investigation the most complete results were obtained for batch 6. The original data points are listed in Table 3.2, and shown in Fig. 3.6 with tensile stress plotted versus compressive stress. The nine original data points, represented by circles, clearly show a gradual decrease in tensile strength as the compressive stress increases. For these tests, however, the tensile direction varied over a range of 80°. Hence, the results should reflect the anisotropy described in the previous section, and a more nearly linear relation might be expected if this anisotropy were somehow accounted for.

Consider what effect anisotropy should have on the data of Fig. 3.6. For panels 48 and 55, the angle between the tensile direction and the normal to the bed joints was 45°, while for panels 50 and 58 the angle was 0°. Hence, by the results shown in Fig. 3.4, panels 48 and 55 can be expected to show less of a decrease in tensile strength compared to panels 50 and 58 than they would if their tensile direction were also 0°.

This observation forms the basis of the following method of correcting the tensile stress of a biaxial test for the known anisotropy in uniaxial tensile strength. The method is illustrated in Fig. 3.7, in which tensile stress is represented by the vertical axis, and compressive stress by the horizontal axis. The circle represents the original data, and is assumed to lie on a line from A, the uniaxial compressive strength, to B, the uniaxial tensile strength for the direction of the tensile stress.

Hence, if the tensile direction is stronger by an amount Δ then the tensile strength for the direction $\theta = 0$, the point would have fallen on the line AC if the specimen had been tested at $\theta = 0$. Thus, the corrected point is represented by x. Anisotropy in compressive strength, if it were known, could be corrected for by the same method.

Since neither A nor B is known until a line is fitted to the data, the correction should be done by an iterative process. But fortunately, the corrections are insensitive to the final result. If one assumes the slope of the line AB, usually about 1/15, the corrected value is determined, and no iterations should be necessary.

For the biaxial tests conducted in this program, the condition of zero head joint normal stress meant that the ratio of compressive stress to tensile stress was determined by the angle at which the tensile stress was applied. Hence, this angle determines the correction Δ in uniaxial strength, and also the final correction in biaxial strength if a slope is assumed for the line AB.

The relation between the ratio of stresses and the tensile direction is

$$r = \operatorname{ctn}^2 \theta ,$$

where r is the ratio of compressive stress to tensile stress, and θ is the angle between the tensile direction and the normal to the bed joints (Fig. 3.8).

If one knows r and Δ, and assumes a slope for the line AB, then the correction δ for the tensile stress is determined as follows. Let the line AB have slope $1/R$. Then the lines AB and AC are given by

$$y = B \left(1 + \frac{x}{RB}\right) ,$$

$$y = (B - \Delta) \left(1 + \frac{x}{RB}\right) .$$

The difference is

$$\delta = \Delta \left(1 + \frac{x}{RB}\right) .$$

Since the original data point lies on the line AB and on the line

$$y = -x/r \quad ,$$

one has

$$x = - \frac{rBR}{r + R} \quad .$$

Substituting this result in the expression for δ gives

$$\delta = \Delta \left(1 - \frac{r}{r + R}\right) \quad .$$

The tests in this program were conducted for six values of the angle θ. Table 3.3 gives the values of θ and the resulting corrections, for $R = 15$. Applying these corrections to the data of Table 3.2 gives the values listed in the last row. These are plotted as x's on Fig. 3.6, and are clearly closer to a straight line than the original data.

A measure of the closeness to a straight line is provided by the methods of statistics [16]. Let the corrected data be represented by the pairs of observations $\{(x_i, y_i); i = 1, 2, \ldots, n\}$, where x_i is the compressive stress $(x_i < 0)$. Assume that the random variable $Y_i = Y|x_i$ is related to x_i by the equation

$$Y_i = \alpha + \beta x_i + E_i \quad ,$$

where the error term E_i is a random variable with mean zero, and that each E_i is normally distributed with the same variance σ^2. Then the regression line

$$\mu_{Y|x} = \alpha + \beta x$$

is estimated by the line

$$\hat{y} = a + bx \quad ,$$

where

$$b = \frac{n \Sigma x_i y_i - (\Sigma x_i)(\Sigma y_i)}{n \Sigma x_i^2 - (\Sigma x_i)^2}$$

$$a = \overline{y} - b\overline{x} \quad ,$$

and the bar over a variable indicates the arithmetic mean. Applying these results to the corrected data gives

$$b = 0.0820$$

$$a = 110.7$$

The accuracy of these estimates of the parameter α and β is expressed by confidence intervals. $(1 - 2\gamma)$ 100% confidence intervals are given by

$$a - \frac{t_\gamma s \sqrt{\Sigma x_i^2}}{\sqrt{n S_{xx}}} < \alpha < a + \frac{t_\gamma s \sqrt{\Sigma x_i^2}}{\sqrt{n S_{xx}}}$$

$$b - \frac{t_\gamma s}{\sqrt{S_{xx}}} < \beta < b + \frac{t_\gamma s}{\sqrt{S_{xx}}} \quad ,$$

where t_γ is a value of the t distribution with $n - 2$ degrees of freedom,

$$S_{xx} = \Sigma x_i^2 - \frac{(\Sigma x_i)^2}{n} \quad ,$$

and s^2 is an unbiased estimate of σ^2 given by

$$s^2 = \frac{[\Sigma y_i^2 - (\Sigma y_i)^2/n] - b[\Sigma x_i y_i - (\Sigma x_i)(\Sigma y_i)/n]}{n - 2} .$$

For the corrected data one finds

$$s = 10.4 ,$$

and 90% confidence intervals are

$$101.1 < \alpha < 120.3$$

$$0.0604 < \beta < 0.1036 .$$

For the purpose of predicting the strength at a particular compressive stress, one has the $(1 - 2\gamma)$ 100% confidence interval for a single response

$$\hat{y}_o - t_\gamma s \sqrt{1 + \frac{1}{n} + \frac{(x_o - \bar{x})^2}{S_{xx}}} < y_o < \hat{y}_o + t_\gamma s \sqrt{1 + \frac{1}{n} + \frac{(x_o - \bar{x})^2}{S_{xx}}} .$$

The 90% confidence intervals at several values of compressive stress are given in Table 3.4.

The line determined by the above procedure is shown in Fig. 3.6. It fits the data quite well, and the confidence intervals give the variability in strength one can expect.

For use in computations, it is necessary to have an expression for the above law of biaxial strength. The statement of this law is quite simple in terms of principal stresses. Let the principal stress σ'_{22} be positive (tensile), σ'_{11} negative (compressive). Then fracture occurs when

$$\sigma'_{22} = \frac{\sigma_t}{\sigma_c}(\sigma'_{11} + \sigma_c) \quad , \qquad (3.2)$$

where σ_t is the uniaxial tensile strength for the x'_2 direction.

The quantity σ_c requires some consideration. If the linear law held for arbitrarily large compressive stress, σ_c (> 0) would be the uniaxial compressive strength for the x'_1 direction. However, the tests in this investigation did not cover the high compressive stress range, and for concrete the uniaxial strength is significantly less than the quantity needed in the above formula (see Fig. 3.5). Hence, σ_c is to be determined from the data fit for the biaxial tests, rather than from uniaxial tests. The behavior in the high compressive stress range is a subject that requires further investigation.

For some purposes it is more convenient to express the first-cracking law in terms of stress components for the joint coordinate system. Let (x_1, x_2) be the joint coordinates, and (x'_1, x'_2) the principal stress coordinates, as in Fig. 2.2.

The two stress invariants are then represented by the following equations:

$$\begin{aligned} \sigma_{11} + \sigma_{22} &= \sigma'_{11} + \sigma'_{22} \\ \sigma_{11}\sigma_{22} - \sigma_{12}^2 &= \sigma'_{11}\sigma'_{22} \end{aligned} \qquad (3.3)$$

Substituting the first of these in Eq. (3.2) gives

$$\sigma'_{11} = \frac{\sigma_c}{\sigma_t + \sigma_c} (\sigma_{11} + \sigma_{22} - \sigma_t)$$

$$\sigma'_{22} = \frac{\sigma_t}{\sigma_t + \sigma_c} (\sigma_{11} + \sigma_{22} + \sigma_c) \qquad (3.4)$$

Substituting Eqs. (3.4) in the second of (3.3) gives

$$\sigma_{11}\sigma_{22} - \sigma_{12}^2 = \frac{\sigma_t \sigma_c}{(\sigma_t + \sigma_c)^2} (\sigma_{11} + \sigma_{22} - \sigma_t)(\sigma_{11} + \sigma_{22} + \sigma_c) , \qquad (3.5)$$

where σ_t is the uniaxial tensile strength in the direction of the principal tensile stress. This strength is given by Eq. (3.1), and the angle needed in (3.1) between the x_2 direction and the direction of the principal tensile stress is

$$\theta = \left| \frac{1}{2} \tan^{-1} \frac{2\sigma_{12}}{\sigma_{11} - \sigma_{22}} - 90° \, H(\sigma_{11} - \sigma_{22})[2H(\sigma_{12}) - 1] \right| , \qquad (3.6)$$

where

$$H(x) = \begin{cases} 1, & x > 0 \\ 0, & x \leq 0 \end{cases} .$$

Equations (3.2) and (3.5) apply only to stress states whose principal stresses are of opposite signs. And while they may hold as long as this condition is satisfied, their validity was checked only for the special case $\sigma_{11} = 0$. The test results and the curve represented by Eq. (3.5), for $\sigma_{11} = 0$, are shown in Fig. 3.9.

3.4 Test Case for Biaxial Law

Once the elastic behavior of a material, and the stress states at which fracture occurs are known, it is possible to predict the load at which a structure will first suffer fracture. In general, it is more difficult to predict the maximum load that can be sustained, for it is necessary to know the post-fracture behavior of the material, and to perform the non-linear analysis required once cracking begins.

In order to see if first fracture could be predicted for non-homogeneous loading, a test was chosen for which the first-fracture and ultimate loads were expected to coincide, so that the first-fracture load could be accurately determined. The test is known as a diagonal compression test, in which a square is loaded at opposite corners, as shown in Fig. 3.10.

For an isotropic linear elastic material under point loads, an analytical solution for the stress state is available. This solution predicts a region of nearly uniform tensile stress at the center of the square in the direction perpendicular to the direction of loading (Fig. 3.10). Since masonry is weak in tension, fracture is expected to begin at the center and propagate toward the loaded corners, with a resulting drop in load.

There are several items that need to be considered in the analysis of this test. One is that the point loads of the analytical solution must actually be distributed loads. For our specimens, the loads were applied through steel caps that extended about 10 inches along the sides from the corners. In order to account for this difference with theory, a finite element computer analysis was performed to predict the stress state for linear elastic behavior. This analysis should also have accounted for the anistropic elastic behavior of masonry. However, at the time the analysis was performed, the complete anisotropic constitutive law was not known, so an isotropic law was assumed.

The final item to be considered is the size of the specimen compared to the block size. The constitutive and fracture laws are expected to apply to nonhomogeneous stress states for which the stresses vary little over a block dimension. The specimens tested were 64 inches on a side (Fig. 3.11). According to the above solution, the stress could vary by as much as 40 percent over the length of a block at the center of the specimen, which is somewhat more variation than is desirable.

The finite element analysis predicted a ratio of compressive stress to tensile stress at the center of 3.45. Homogeneous tests had been performed with a ratio of 3.00, so the same orientation was used in the diagonal compression test, and the biaxial fracture law was used to correct for the difference in stress ratios. The predicted failure loads agree quite well with the test results, as shown in Table 3.5.

3.5 Strength of Reinforced Masonry

The strength of masonry at first fracture is expected to be little influenced by steel reinforcing in the amount used in the specimens tested in this investigation. The fractional steel area of 0.00126, which exceeds minimum UBC requirements, is so small that at the strains at which masonry fracture occurs, the steel is carrying an extra load equivalent to only about 4 psi. Hence, reinforced masonry should be only slightly stronger at first cracking, and the biaxial results determined for unreinforced masonry should still hold.

A test of this hypothesis is available in the data from batch 8. Several tests were conducted for both reinforced and unreinforced specimens at lay-up angles of 0° and 80°. The results are given in Table 3.6.

It is seen that the reinforced specimens are stronger by about 25 percent, which is a somewhat greater increase than expected. Though this is a small sample for making a comparison, the results are consistent enough to suggest that somehow the steel postpones the onset of cracking. Until more data is available to check this increase in strength, however, masonry with this amount (or less) of reinforcing steel should be considered to have a first-cracking strength equal to that of unreinforced masonry.

3.6 Strength Prediction

It is clearly desirable to be able to predict the strength of masonry from the properties of its components. This ability would enable one to select components that would produce the strongest possible assemblage, and would reduce the amount of testing necessary for a new combination of components. The problem is a complex one, but these experiments have provided some knowledge of the internal mechanisms that influence strength.

The stress state for which the behavior is simplest, and strength prediction has the best chance of success, is uniaxial tension across the bed joints. The strength for this case is expected to be determined primarily by the strength of the grout, because joint tests have shown [17] that the mortar bonds have little or no tensile strength. Multiplying the grout cross-sectional area by the grout tensile strength gives the maximum load that can be sustained if the mortar bond has no strength. This load divided by the entire masonry cross-sectional area then represents the predicted tensile strength.

The grout strength and two panel strengths are available for batch 6. The results are given in Table 3.7, and the predicted strength is seen to be in excellent agreement with the test results.

This method of predicting tensile strength would, unforunately, give poor agreement in many cases, due to flaws in the grout. Examination of failed specimens and the edges of panels cut from walls has revealed that most specimens suffer grout flaws and grout-block separation. There is frequently a regular pattern of flaws at the bed joints (Fig. 3.12). These grout bridges apparently result from the restrictions created by the change in block wall thickness and the slight intrusion of mortar into the grout cell.

The seriousness of these flaws will clearly be influenced by such factors as grout viscosity and compaction, and curing conditions. It was found that for batch 6, which cured during an exceptionally wet period, flaws were almost nonexistent. This is the reason for the excellent agreement in Table 3.7, and for the consistently high strengths recorded for batch 6.

A striking illustration of the influence of flaws on strength is available in a tensile test of a prism whose fracture surface clearly shows a flawed region. The intact grout, whose surface was distinguishable by a difference in color and texture, is represented by the cross-hatched region in Fig. 3.13. The remaining area represents a flaw that was incapable of carrying load. The ratio of intact grout area to the total grout area was 0.67. This reduced area, multiplied by the grout strength, gave a predicted strength within a few percent of the actual failure load. It is thus clear that the ability to predict tensile strength across the bed joints requires a knowledge of the size of the grout flaws.

For a tensile test in the opposite direction, that is, with tension across the head joints, the fracture pattern is more complicated. For this stress state the obvious weak point is the head joints, and the fracture invariably follows a path through a set of head joints. Between head joints, the fracture generally runs through the center of a block, just to one side of the web, as shown in Fig. 3.14.

The stress for this loading is thus carried by three regions: the head joint, the two face shells of the block, and the area of contact between the web and the grout. Tests have shown that the head joints possess little tensile strength, and the load required to fracture the face shells can be predicted, so the only remaining area is that of contact between web and grout.

Examination of failed specimens from batch 6 showed that roughly a third of the web area had been adhered to by the grout. The remaining area suffered separation during construction or curing. Addition of the load required to fail one third of the web area to the load needed to fail the face shells gives a predicted failure stress of 83 psi. The average strength for two specimens from batch 6 was 95 psi, which is in fair agreement with the prediction.

It is thus clear that a knowledge of component strengths is not sufficient to predict the strength of the assemblage. One must also know the extent of flaws and grout separation. Further, if flaws could be eliminated and the grout made to adhere to the block, the resulting masonry would be substantially stronger.

The analysis of strength in this section was limited to two special cases. The other stress states, which are tension at an arbitrary orientation, compression, and biaxial stress, are more complicated and are not yet understood. Insight into the failure mechanisms for these cases would represent important progress in the understanding of masonry behavior.

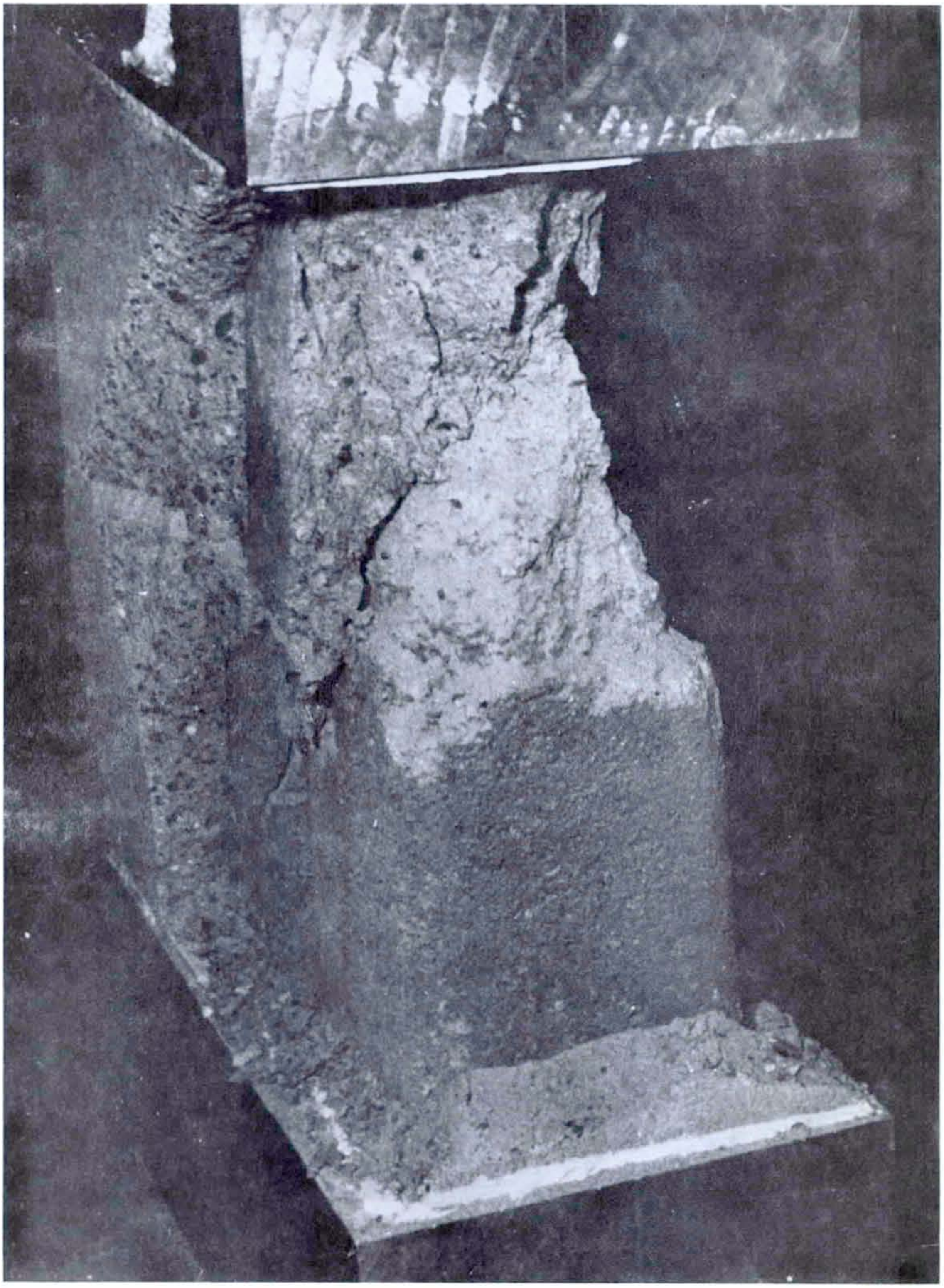

Fig. 3.1. End Restraint in Two-Course Prism with Hard Cap

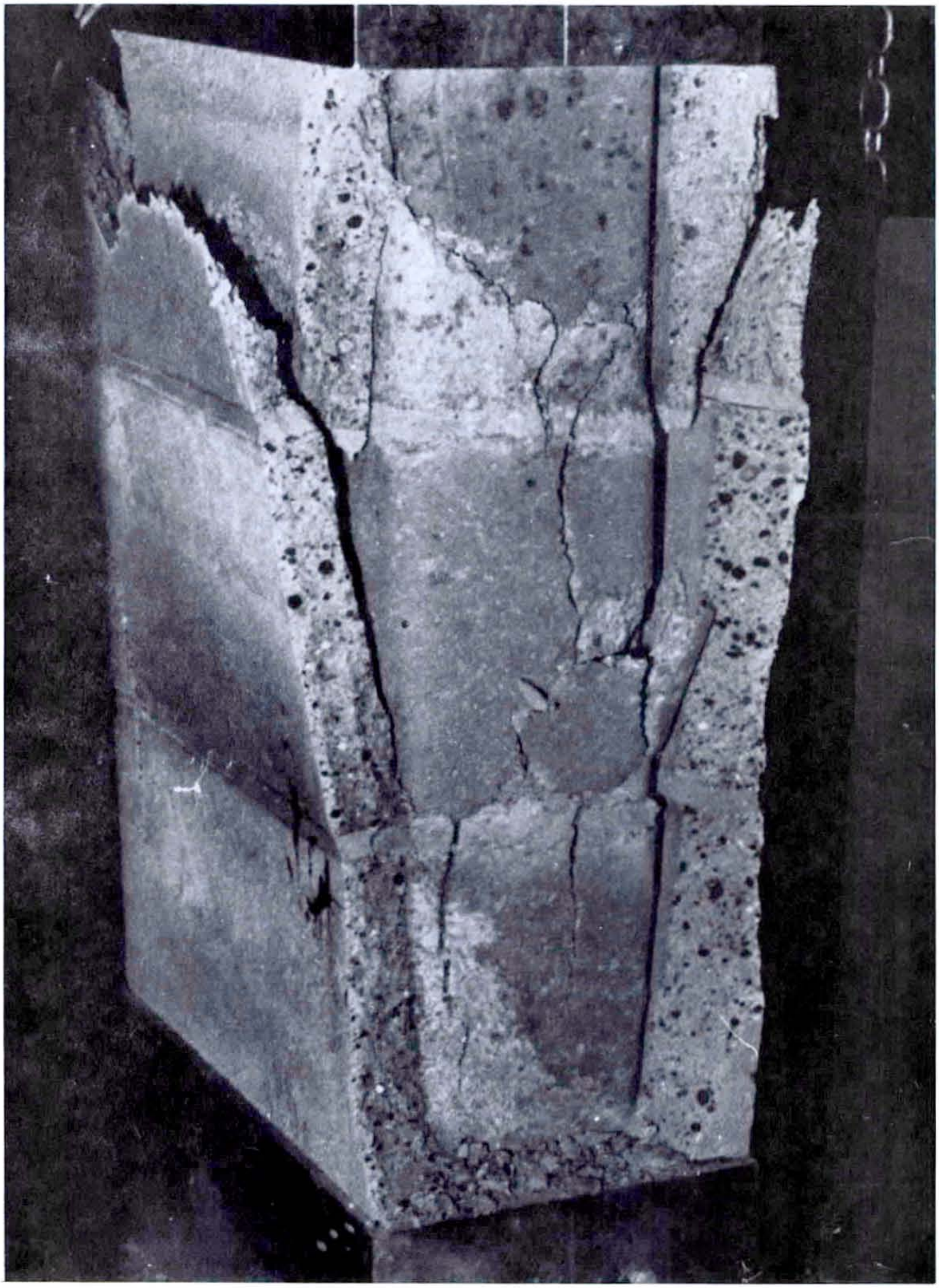

Fig. 3.2. Tensile Splitting of Three-Course Prism

Fig. 3.3. Tensile Splitting of Two-Course Prism with Soft Cap

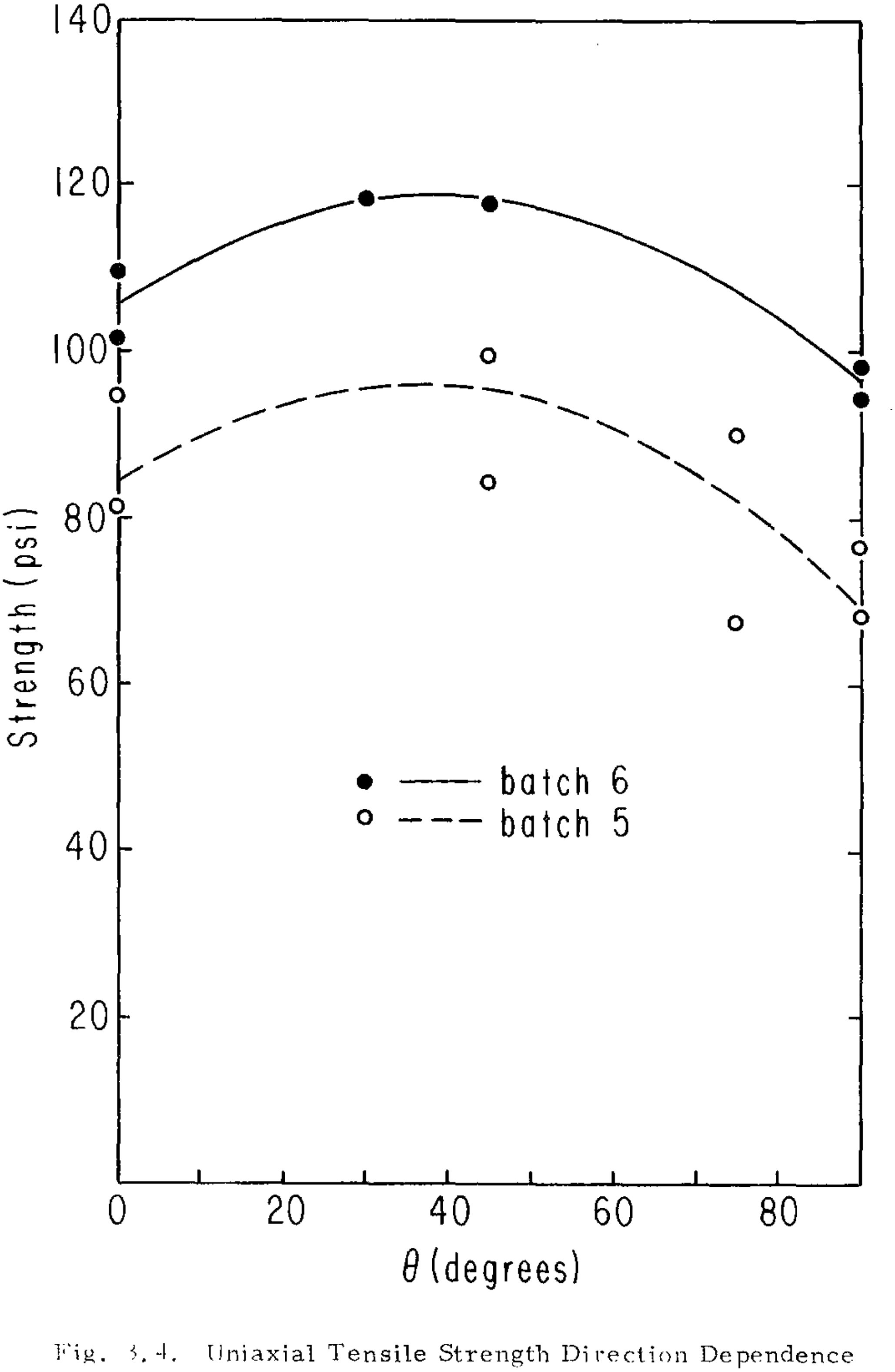

Fig. 3.4. Uniaxial Tensile Strength Direction Dependence

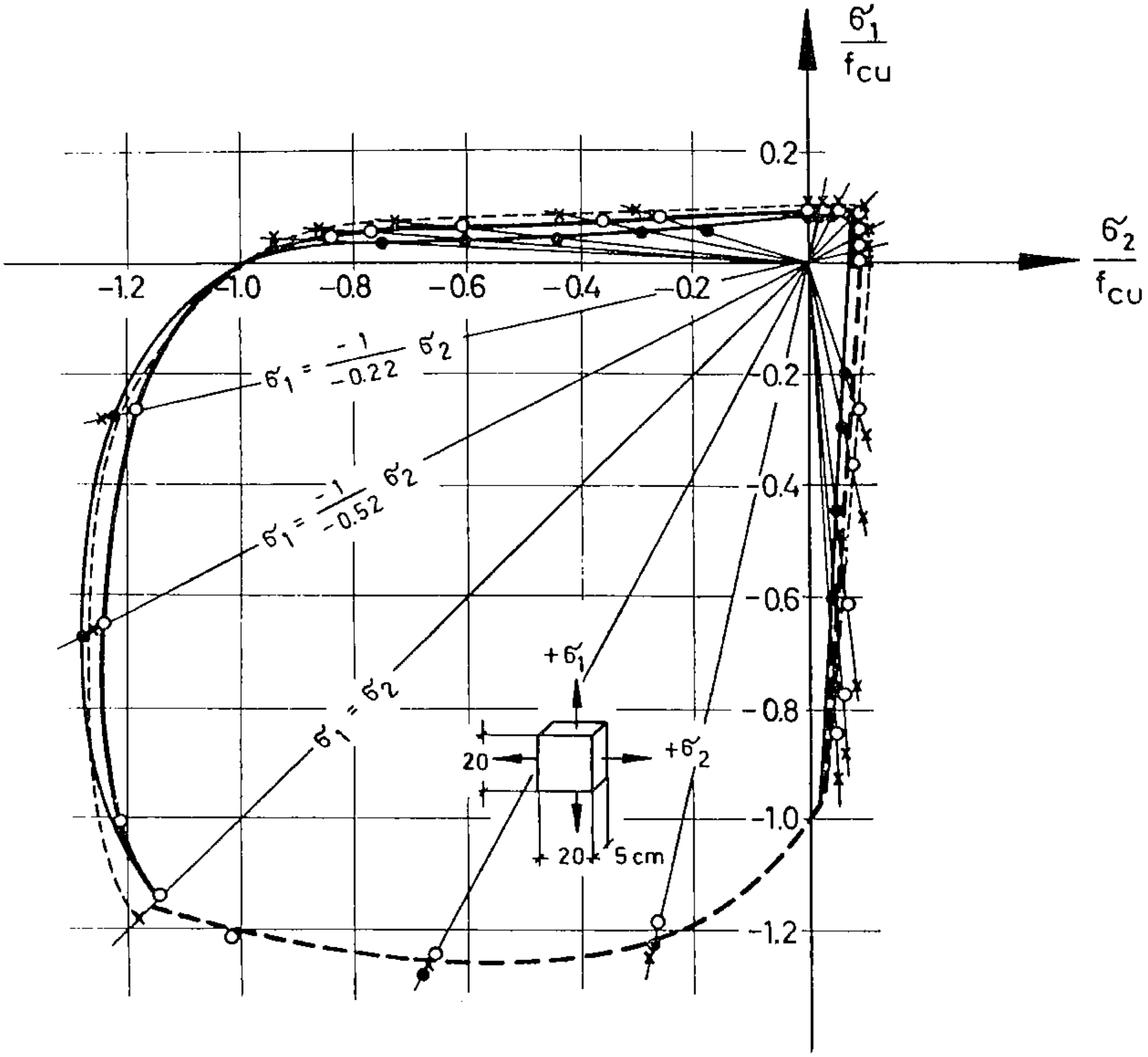

Fig. 3.5. Biaxial Strength of Concrete, from [9]

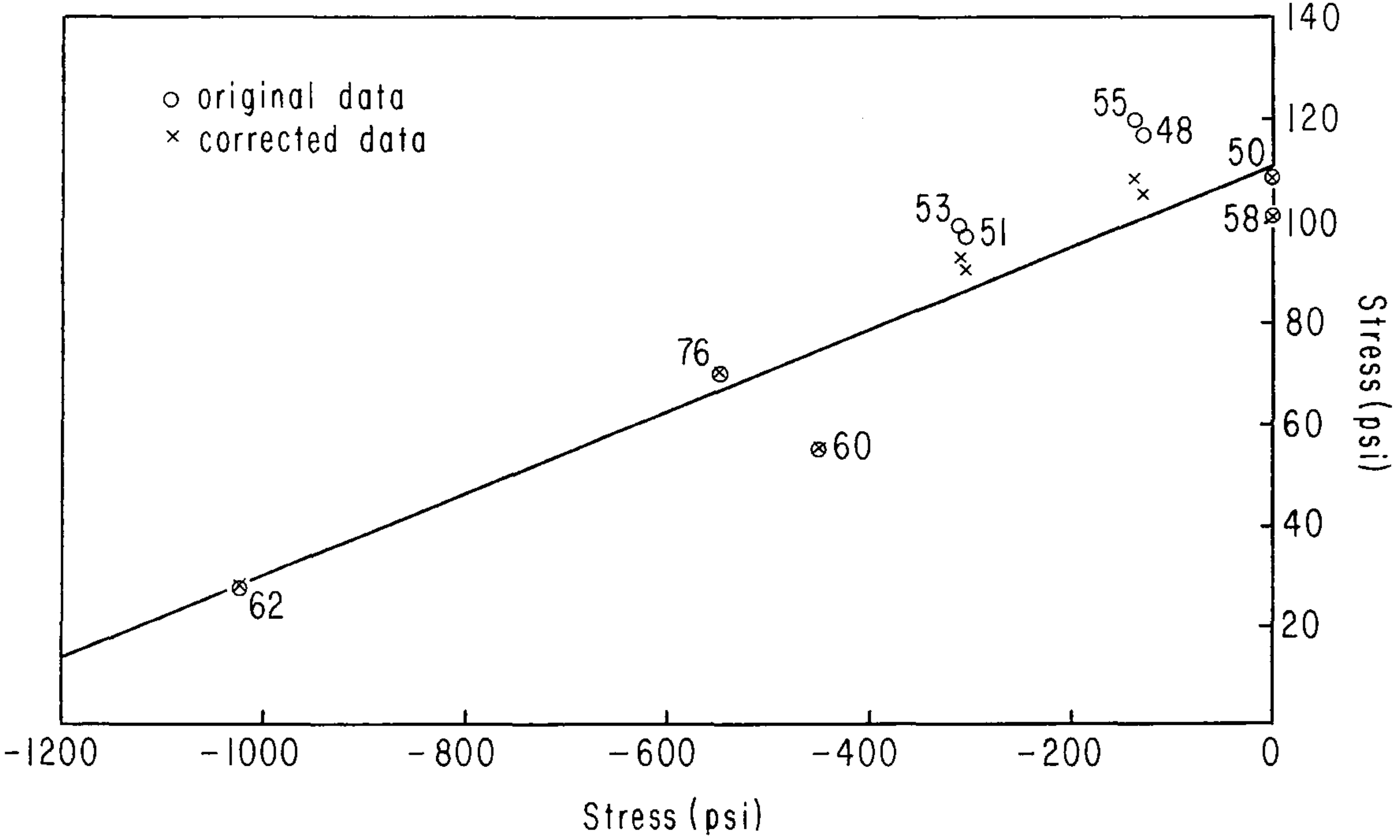

Fig. 3.6. Biaxial Strength of Batch 6

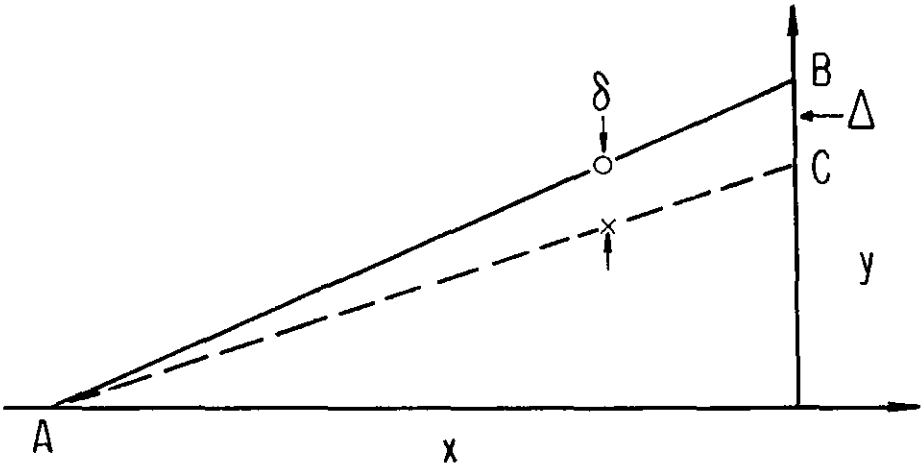

Fig. 3.7. Correction of Biaxial Stress for Anisotropy

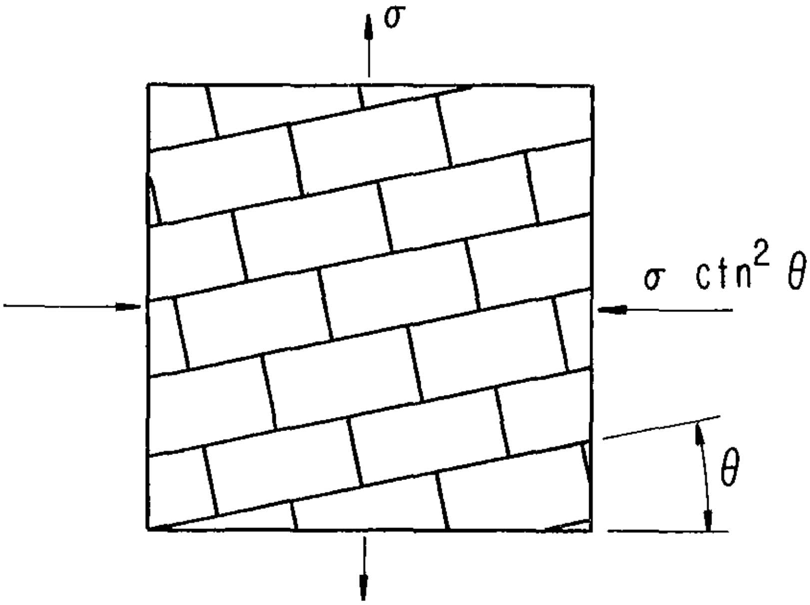

Fig. 3.8. Relation of Lay-up Angle to Stress Ratio

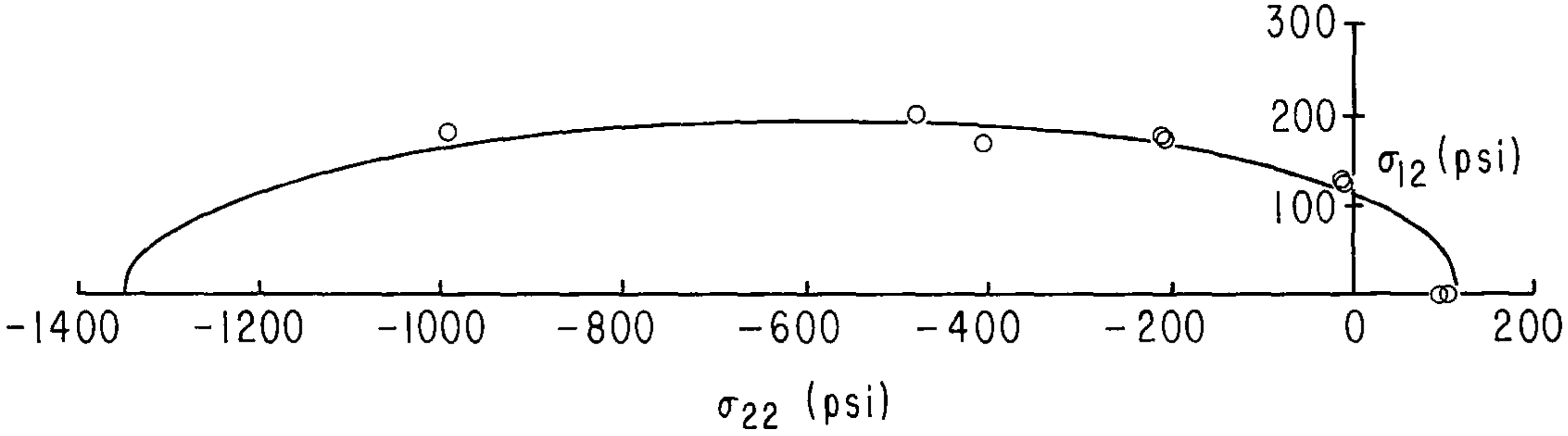

Fig. 3.9. Shear Strength versus Compressive Stress, Batch 6

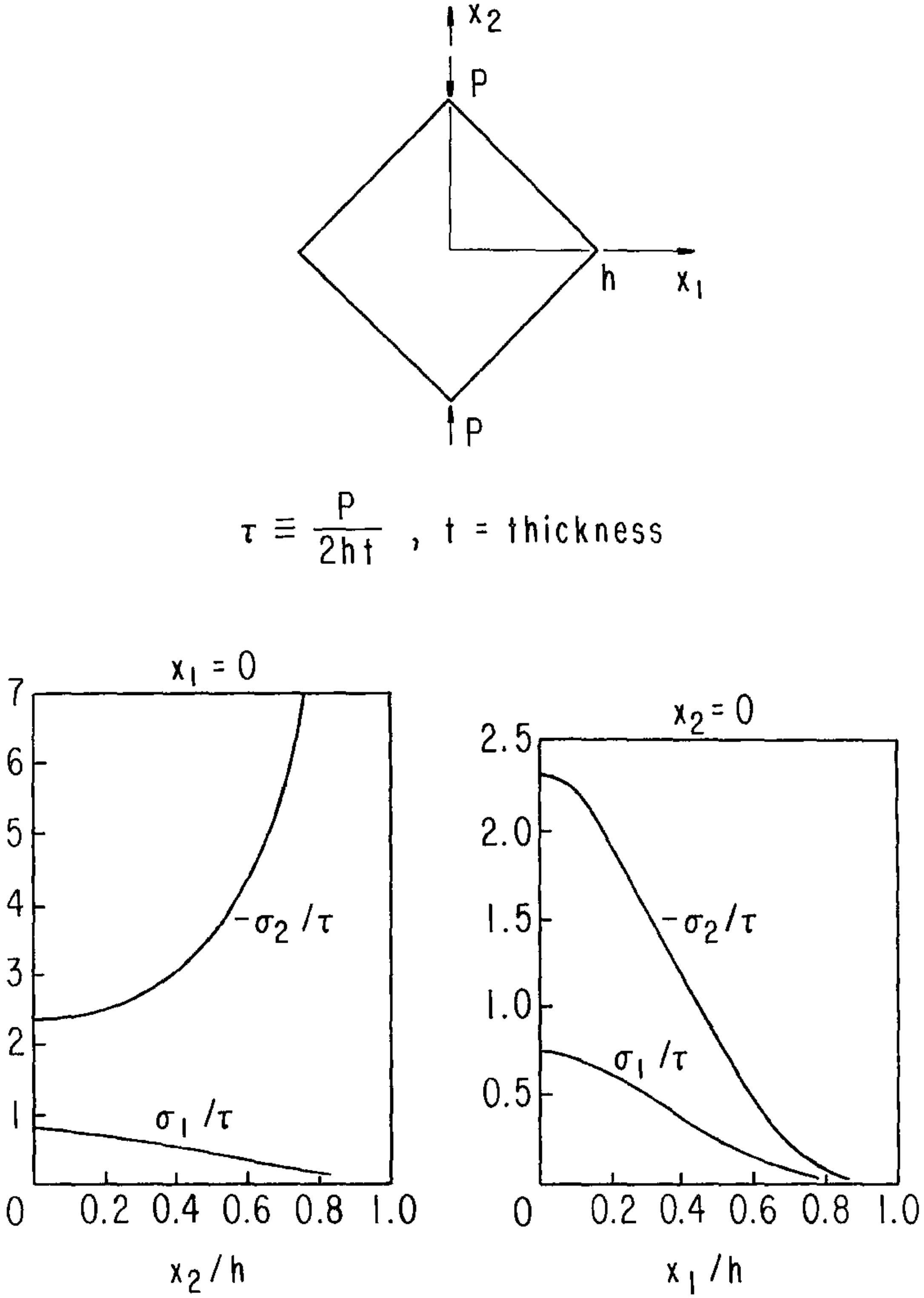

$$\tau \equiv \frac{P}{2ht} \quad , \quad t = \text{thickness}$$

Fig. 3.10. Diagonal Compression Test and Stresses along Diagonals

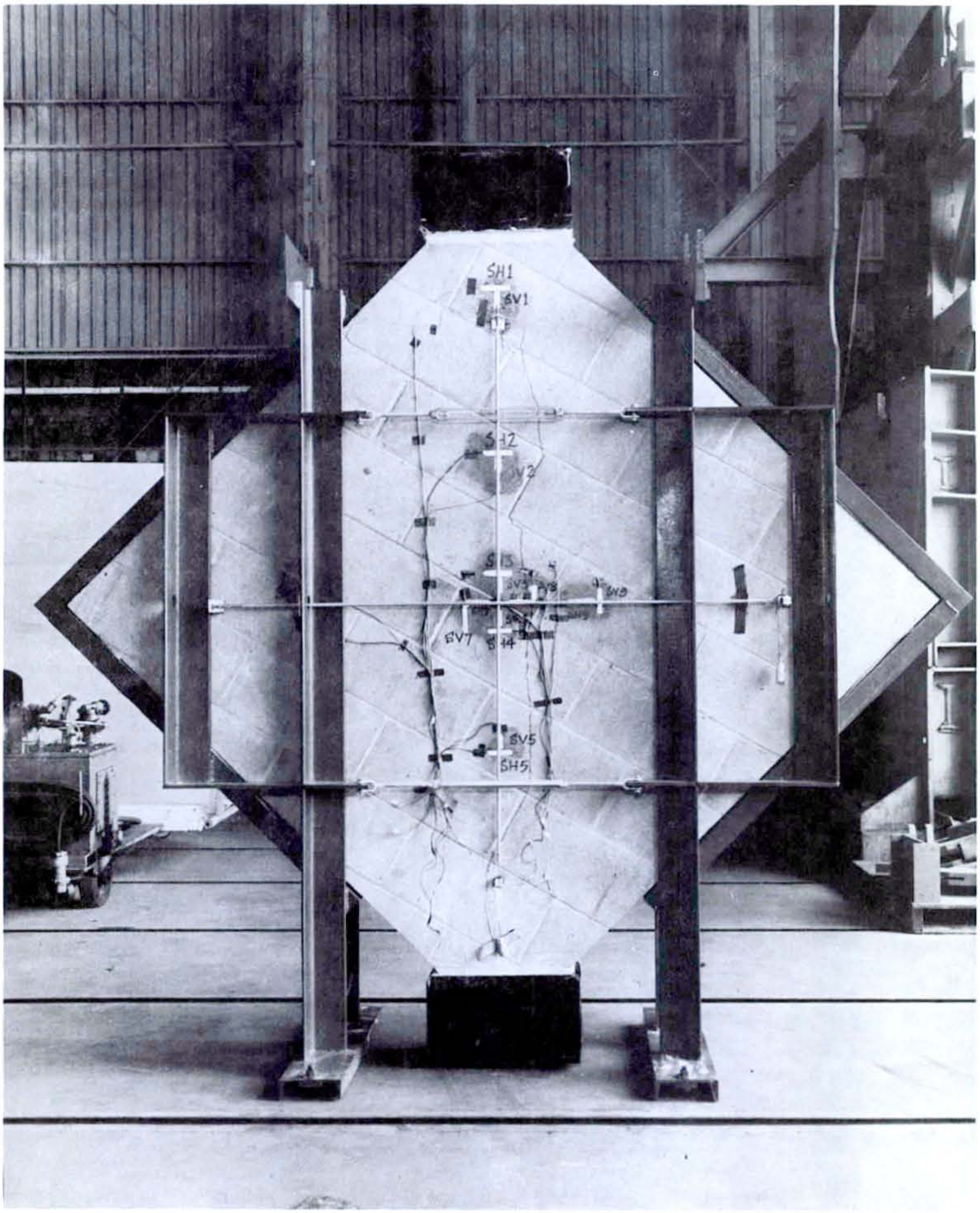

Fig. 3.11. Typical Diagonal Compression Test Fracture

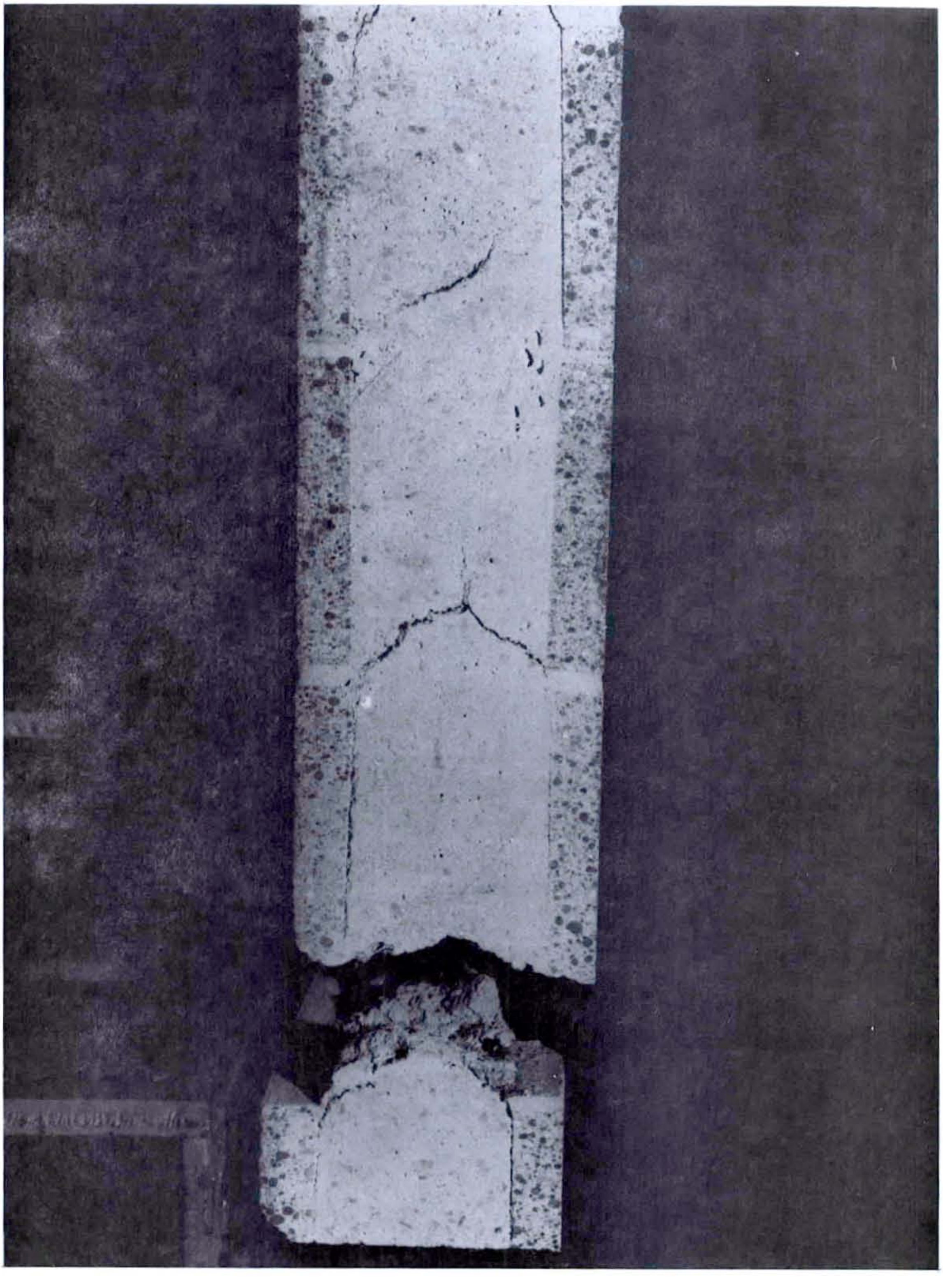

Fig. 3.12. Grout Bridges and Resulting Failure

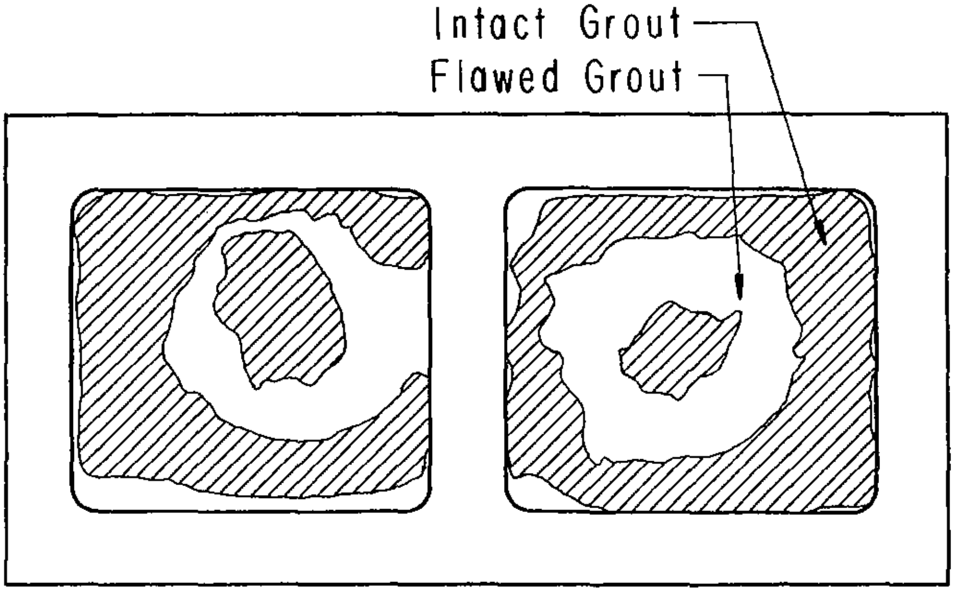

Fig. 3.13. Grout Flaws at Bed-Joint Plane

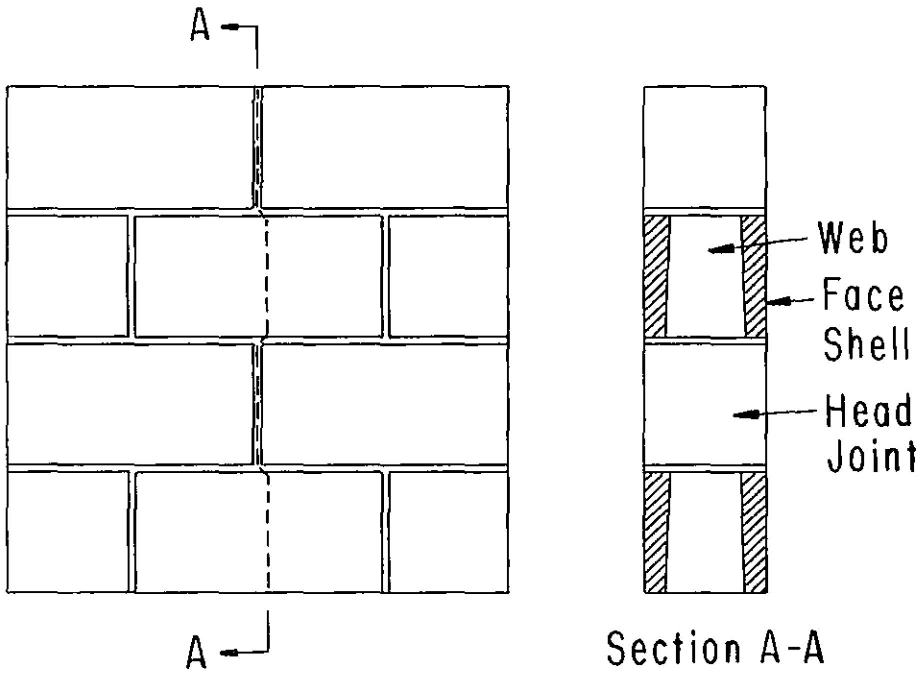

Fig. 3.14. Head-Joint Fracture Path

Table 3.1. Coefficients of Uniaxial Tensile Strength Quadratic

	$\sigma_t^{(0)}$	a	b
Batch 5	84.3	0.660	-0.00924
Batch 6	105.5	0.677	-0.00871

Table 3.2. Biaxial Failures Stresses (psi) for Batch 6

θ	0	45	60	70	80
Compr. stress	0	-128	-305	-446	-1023
Orig. tensile stress	109	117	97	55	28
Corrected stress	109	106	91	53	29
Compr. stress	0	-136	-309	-548	
Orig. tensile stress	101	120	99	70	
Corrected stress	101	109	93	68	

Table 3.3. Correction of Tensile Stress for Anisotropy

θ	r	Δ (psi)	δ (psi)
0	0	0	0
45	1.00	11.9	11.2
60	3.00	7.8	6.5
70	7.55	2.8	1.9
75	13.9	-0.4	-0.2
80	32.2	-4.0	-1.3

Table 3.4. Single Response 90% Confidence Intervals

Compr. Stress (psi)	0	-200	-400	-600	-800	-1000
Tensile stress interval (psi)	133	115	99	83	68	54
	89	73	57	40	22	3

Table 3.5. Diagonal Compression Test Failure Loads (10^3 lb)

Predicted Values	105.9	78.2
Test results	107.3	83.4
		89.7

Table 3.6. Comparison of Unreinforced and Reinforced Strengths (psi)

		Unreinforced			Reinforced	
θ	Panel #	σ'_{11}	σ'_{22}	Panel #	σ'_{11}	σ'_{22}
0	85	0	78	80	0	99
	91	0	64	83	0	88
				87	0	91
	avg.	0	71	avg.	0	93
80	79	49	-357	82	63	-441
	84	52	-395	86	62	-482
				92	63	-465
	avg.	50	-376	avg.	63	-463

Table 3.7. Tensile Strength Prediction (psi)

Grout Strength	Predicted Panel Strength	Panel Test Results
206	103	109
		102

CHAPTER 4. POST-FRACTURE BEHAVIOR

The behavior of masonry following initial fracture is of great importance for a structure subjected to strong seismic loading. If the material possesses some ductility and can sustain a significant part of its original load following fracture, the chances of survival of the structure will be greatly improved. Grouting and steel reinforcing will help to insure the integrity of the material after cracking begins, and the energy absorbed during ductile deformation can be an important source of damping.

The description of masonry behavior once cracking begins is, of course, very difficult, and no well developed theory exists which can accurately predict this behavior. Some of the complexities are load drop at first fracture, stiffness degradation, crack closure, and path dependence. For the case of steel-reinforced masonry, some success has been had with plasticity models. This success was hoped for, since the post-fracture behavior is determined largely by the reinforcing steel, and steel is a material for which the plasticity theory works very well.

4.1 Subsequent Loading Surfaces

The failure surface discussed in the previous chapter consists of the stress states at which fracture, and non-linear behavior, commence. Once the material has fractured, it is convenient to have a similar surface, called a subsequent loading surface, that represents the maximum load that can be sustained. Stresses below this surface usually cause little further cracking, and behavior below this surface is generally linear, though reinforced specimens exhibit a large increase in stiffness on transition from tensile to compressive loading.

Upon reloading, the stress-strain curve levels off suddenly as it approaches the loading surface, as shown in Fig. 4.1. The loading surface may suffer a sudden drop at the first tensile fracture, as shown with a different strain scale in Fig. 4.2, and continued deformation associated with stresses on the surface usually causes further cracking, and can cause the surface to change.

Determination of this changing surface is clearly a difficult task. The variety of possible loading paths makes a strictly experimental determination for all cases nearly impossible. The only chance of success is to restrict attention to a limited number of cases, and then to combine experimental results with some understanding of the structure of the material.

Consider first what occurs as cracking begins, for a uniaxial stress state. For uniaxial compression the only data available is that from prism tests, which are described in Section 3.1. As discussed in that section, the behavior of running-bond prisms of more than three courses is expected to correspond closely to that of full-scale masonry.

As shown in Fig. 4.3, the stress-strain curve for a prism compression test has a large linear section, then the load continues to climb a small amount before beginning to drop. The end of the linear part of the curve is believed to mark the onset of cracking. It is this stress, then, that represents a point on the initial yield surface. As deformation continues, this part of the surface expands a small amount, then begins to contract.

The effect of this cracking on other parts of the surface can only be surmised. The grout cores are known to remain intact until well after cracking begins, so the tensile strength probably drops slowly. Gradual disintegration of the material likely causes strength in the opposite direction to decrease: Once the face shells have broken off there can be little strength left across the head joints. Compressive behavior is probably very similar for reinforced and unreinforced masonry.

For the case of uniaxial tension, the behavior depends strongly on whether or not the material is reinforced. The load of an unreinforced specimen drops immediately to zero at the onset of cracking. As shown in Fig. 4.4, the behavior is linear up to the load drop. A reinforced specimen, on the other hand, is able to sustain some load following a sudden drop in load, as shown in Fig. 4.2.

This reduced load must be transmitted across the crack by the reinforcing steel. At the point where the load levels off in

Fig. 4.2, the strain is about 9×10^{-5}, while the stress is 50,000 psi. If the steel, whose total area is 0.61 in^2, were strained uniformly, it would carry a load corresponding to a stress of only 3,000 psi. Hence, its load is being transmitted to the masonry. Since the load drops by 40 percent at first cracking, either the masonry suffers some debonding, or the wide steel spacing allows a large section of masonry to remain unloaded. If there were more reinforcing, the load would be transmitted more effectively, and the drop in load might be nearly eliminated.

As the strain continues to increase, the load gradually climbs. Because we were interested in cyclic and reloading behavior, none of the specimens tested in this investigation were loaded monotonically to large strain. However, the envelope for the cyclic curves is believed to be very close to the monotonic curve. As seen in Fig. 4.2, there is an abrupt change in slope as a reloading curve reaches this envelope. This change in slope is associated with the continuation of cracking. Hence, an unloading cycle below this envelope should have little effect on the behavior of the material, and the envelope should represent the monotonic loading curve.

As the strain increases further, the stress is seen to level off. On Fig. 4.1, the stress corresponding to yield of the 60,000 psi reinforcing steel has been indicated. It is seen that at large strain the load is just the maximum load that can be sustained by the yielded steel. For reinforced specimens this large strain produces numerous cracks, as shown in Fig. 4.5, because of the load transmitted by the steel.

Once the material has cracked, its tensile strength becomes very direction dependent. While the strength across the crack drops to a level that depends on the amount of reinforcing steel, the strength in the direction parallel to the crack is probably unaffected. Further, the strength in compression is probably affected little by tensile cracking. Figure 4.2 shows that as a cracked specimen is compressed, the load increases sharply, due to the closing of cracks.

Once these cracks have closed, the specimen is probably able to sustain a load close to its unfractured compressive strength. However, the extensive cracking associated with large strain of a reinforced specimen is likely to cause a general reduction in strength.

This completes the discussion of post-fracture strength for uniaxial stress, except for dependence on crack direction, which was not studied. So there remains the strength under biaxial loading. Because such a large variety of biaxial stress states are possible, knowledge of such behavior is rather sketchy. No tests were conducted under biaxial tension or compression, so little is known about these cases.

Since the biaxial tests that were conducted all had one principal stress tensile, the tests of unreinforced specimens ended at first cracking, for the crack meant that a tensile load could no longer be sustained. For the reinforced specimens, the loading was continued well past first cracking. The loading in these tests was proportional, with a constant ratio of compressive to tensile stress throughout the test. Thus, as cracking began and the tensile stress dropped, the compressive stress was reduced.

Reinforced biaxial tests were conducted at two lay-up angles (as defined in Section 3.3): 45°, with a compressive to tensile stress ratio of 1 to 1; and 70°, with a ratio of 7.5 to 1. Figures 4.6 and 4.7 show the tensile stress versus the corresponding strain for a specimen of each type. A comparison of these two cases with the uniaxial case shown in Fig. 4.1 reveals two items of importance.

First, while there is a load drop as cracking begins for the two biaxial cases, the drop is much less than for the uniaxial specimens. This difference is not well understood, but is likely related to the rather complex crack pattern occurring in the biaxial tests. The initial cracks, marked "1" in Fig. 4.8, fail to cross the specimen completely. Rather, they consist of several isolated short cracks, so that there remain intact segments able to carry load.

These intact segments may survive because at a non-zero lay-up angle both vertical and horizontal reinforcing steel act to prevent cracking. That is, a crack may have to cross three or four bars, instead of just two bars. But this can't be a complete explanation, because the 45° tests show a larger drop than the 70° tests. So it appears that the absence of a large drop in the tensile load must somehow be related to the compressive load in the opposite direction.

The other item to be noted is that at large strain the tensile load has climbed to about the same level (75 psi) for all three cases. For the 0° case, this level is simply the stress corresponding to the ultimate load of the two vertical bars of reinforcing steel. The load approaches this stress quickly, then remains nearly constant.

For the specimens with a lay-up angle different from zero, the behavior at large strain is more difficult to explain. It is seen that the load climbs more slowly, and appears to be still increasing at the largest strain achieved. The reason the load climbs more slowly may be that the steel is able to bend, since it crosses the crack at an angle. And since the crack must cross more bars for these cases, it may be that the maximum load will be higher. The increase would amount to a factor of $\sqrt{2}$ for the 45° case.

These tests thus provide some useful results, but rather meager information for the construction of a post-fracture loading surface. By making some assumptions, however, the task can be accomplished. It will be necessary to remember, of course, that a result of such guessing will be limited accuracy on some parts of the surface. Since there is no information on biaxial compression, this part of the surface will not be described.

It is useful to make some idealizations of the data represented by the loading curves of Figs. 4.1, 4.6, and 4.7. First, the stress will be assumed to drop with no change in strain at first fracture, to the same level, 55 psi, for all values of compressive stress. (If the compressive stress is high enough that fracture occurs at a tensile stress less than 55 psi, there will be no stress drop. It will be assumed that the material simply hardens at the same rate as in other cases.) Second, though the stress for the 45° test shows a tendency to climb, it will be assumed that the stress at large strain is the same, 75 psi, for all conditions. Finally, it will be assumed that the rate of hardening (the increase of tensile stress with tensile strain) following fracture is always 1.5×10^5 psi. Thus, if e_t is the tensile strain across the crack, and σ_t is the corresponding tensile strength, one has

$$\frac{d\sigma_t}{de_t} = 1.5 \times 10^4 \text{ psi}, \quad \sigma_t < 75 \text{ psi} \quad . \tag{4.1}$$

Though there were some variations in the tensile stresses immediately following fracture, and at large strain, they were small. It therefore appears that the tensile strength after first fracture must be independent of the compressive stress, in contrast to the situation before fracture. But this is a reasonable result, since the strength is due primarily to the reinforcing steel, which should be little affected by compression perpendicular to its length.

Once the material has fractured, it is convenient to describe behavior in terms of a coordinate system aligned with the crack. Let this coordinate system be unprimed, and let primed coordinates at an angle θ represent a hypothetical principal stress orientation (Fig. 4.9). In the experiments the crack direction was always a principal stress direction, but it is necessary to be able to consider an arbitrary stress state.

Let x_2' be in the tensile direction, and let σ_t' and σ_c' represent the tensile and compressive strengths in the x_2' and x_1' directions. It will be assumed that the linear relation between tensile and compressive stresses still holds. That is, for a compressive stress σ_{11}', a point on the loading surface will have a tensile stress given by

$$\sigma_{22}' = \sigma_t' \left(1 + \frac{\sigma_{11}'}{\sigma_c'}\right) \quad . \tag{4.2}$$

As noted above, tensile strength in the x_2 direction should be independent of the compressive stress σ_{11}. In the above equation, this can be achieved by letting σ_c' go to infinity when x_1' coincides with x_1. When $\theta = 90°$, so that the compressive direction x_1' is normal to the crack, the crack will be closed, so that σ_t' and σ_c' should have their pre-fracture values. Formulas that vary smoothly between these two cases are

$$\begin{aligned} \sigma_t' &= \sigma_t + (\sigma_t^o - \sigma_t) \sin^2\theta \\ \sigma_c' &= \frac{\sigma_c^o}{1 - \cos\theta} \end{aligned} \quad , \tag{4.3}$$

where σ_t^o and σ_c^o are the pre-fracture strengths, and σ_t is the post-fracture tensile strength described above. Since the compressive stress cannot be arbitrary, the condition $\sigma_{11}' > -\sigma_c^o$ must be added to (4.2).

If (4.2) is rewritten in terms of the unprimed stress components (as was done in Section 3.3), one obtains for the loading surface

$$\sigma_{12}^2 = \sigma_{11}\sigma_{22} - \frac{\sigma_t'}{\left(1 + \frac{\sigma_t'}{\sigma_c'}\right)^2}\left(1 + \frac{\sigma_{11} + \sigma_{22}}{\sigma_c'}\right)(\sigma_{11} + \sigma_{22} - \sigma_t') \, , \tag{4.4}$$

where σ_t' and σ_c' are given by (4.3), and the magnitude of θ is given by Eq. (3.6).

Equation (4.4) applies in each of the two quadrants in which the principal stresses are of opposite sign. Data from concrete suggests that for biaxial tension, the strength in each direction is independent of the other stress. Hence, each tensile strength should be given by the corresponding value of σ_t' from (4.3). Biaxial compressive behavior is unknown.

4.2 Stiffness Degradation

The loading surface discussed in Section 4.1 describes the stresses that fractured masonry can support. Analysis of a structure requires in addition a knowledge of the displacements associated with stresses both on and below the loading surface. Behavior of reinforced masonry below the surface is the subject of this section.

As mentioned in Section 4.1, little further cracking occurs below the loading surface, so the behavior is generally linear. The stiffness depends, of course, on the amount of cracking, and hence can decrease whenever the surface is reached. For the uniaxial tension specimen of Fig. 4.2, the stiffness decreased to about one sixth its original value at first cracking, and Fig. 4.1 shows continued decrease at large strain.

Further, the linearity is only approximate, and holds only within certain regions. Figure 4.2 shows that crack closure associated with transition from tensile to compressive stress increases stiffness to nearly the uncracked level. Therefore, to know the stiffness, one must keep track of the strain in the direction normal to the crack.

It appears, then, the behavior below the loading surface can be treated as linear within each of two regions, which are defined by the condition of crack closure. With the cracks closed, the behavior should be close to the behavior of uncracked masonry described in Chapter 2. With the cracks open, the material becomes highly anisotropic, with stiffness in the direction normal to the crack dependent on the extent of cracking. In fact, the cracked specimen becomes a new material whose properties can be determined by the same sort of analysis employed in Chapter 2. The elastic matrix may be more complicated, however, since material symmetry may be lost (e.g., uniaxial tension applied to a specimen with cracks at 45° may produce shear strain).

The complete determination of this changing elastic matrix will clearly require more data than is available from the experiments of this program, but by combining the data that is available with some simple assumptions, one can produce a matrix that should be accurate enough to be useful.

Reinforced specimens were unloaded and reloaded at several tensile strains following initial fracture. (See, for example, Fig. 4.1.) An examination of the slopes of the tensile stress versus tensile strain paths reveals a gradual decrease in stiffness to a limiting value of about 3.8×10^4 psi, which is just the stiffness due to the two bars of reinforcing steel. (This is the value if the steel is perpendicular to the crack, but the experiments show little variation with crack direction.) This limiting value was reached at approximately the same tensile strain in each of the three tests for which this data is available, so it appears that one should be able to relate stiffness in the tensile direction to the tensile strain.

In order to complete the elastic matrix, some assumptions must be made. The first will be that the compressive stress produces about the same compressive and tensile strains as in the uncracked specimen. The next assumption concerns shear behavior, and is little more than a guess. The shear modulus is certain to decrease with cracking, but there is no data to indicate the rate of decrease. So the second assumption will be that the shear modulus decreases at the same rate as the stiffness in the tensile direction. The final assumption is that the terms relating shear stress to extensional strains are zero. (They must be zero if the crack direction coincides with the reinforcing direction.)

The elastic matrix thus takes the form (in coordinates aligned with the crack direction)

$$\begin{bmatrix} e_{11}^{e} \\ e_{22}^{e} \\ e_{12}^{e} \end{bmatrix} = \begin{bmatrix} 1/D_1 & -\nu/D_1 & 0 \\ -\nu/D_1 & 1/gD_0 & 0 \\ 0 & 0 & 1/2gG \end{bmatrix} \begin{bmatrix} \sigma_{11} \\ \sigma_{22} \\ \sigma_{12} \end{bmatrix} , \tag{4.5}$$

where ν and G are the moduli of the uncracked material, D_0 is a constant, g is the function of strain that describes the rate of stiffness degradation, and D_1 is the stiffness of the uncracked material in the compression direction. The denominator of the Poisson's ratio term is taken to be D_1 so that the stress σ_{11} won't produce a strain e_{22}^{e} larger in magnitude than e_{11}^{e}.

The final step is to determine the function g. Tests were conducted on three specimens at different orientations (0°, 45°, and 70°) and load ratios. If their stiffnesses are plotted versus tensile strain, one finds curves of similar shapes, but offset in strain. Such an offset is suggested independently by the following consideration. If a specimen suffers stiffness degradation at fracture, and is immediately unloaded, the strain e_{22} will become negative if the stiffness is small enough. To prevent such an occurrence, one can require the stiffness at fracture to have just that value that will yield zero tensile strain at zero stress. That stiffness then determines, through the function g, an offset in strain.

The shape of the stiffness degradation curves is about that of $1/e_{22}$. The constant D_0 is needed so that g will have an initial value close to one. Hence, let

$$D_0 = 1.5 \times 10^6 \text{ psi} \quad ,$$

and for small e_{22} let

$$g(e_{22}) = \frac{1}{2.3 \times 10^4 \, (e_{22} - \delta)} \quad , \tag{4.6}$$

where δ is the offset to be determined by the above procedure, and the coefficient 2.3×10^4 was chosen by fitting the data. For large e_{22}, one has $gD_0 = 3.8 \times 10^4$ psi.

For the three specimens that were tested, one can find the strain e_{22} at fracture from the known elastic law and the law for first fracture. This strain is given in the first row of Table 4.1. Since the tensile stress drops at fracture, one has a new value of σ_{22}. With this new value, and the calculated value of e_{22}, Eq. (4.5) then can be solved for gD_0 (given in the second row of Table 4.1). Finally, Eq. (4.6) can be solved for δ, given in the last row of Table 4.1.

Table 4.2 gives the measured stiffnesses for the three specimens, and in Fig. 4.10 these are plotted versus $e_{22} - \delta$. The curve is given by Eq. (4.6) with $\delta = 0$ for small strain, with the constant value 3.8×10^4 psi for large strain, and is seen to represent the data quite well.

4.3 Anelastic Strain

A knowledge of the elastic strain discussed in Chapter 2 is needed for one to predict the commencement of fracture. But this strain, and even the elastic strain associated with the reduced stiffness of the above section, can be small compared to the anelastic strain. Therefore, a theory that relates anelastic strain to the state of stress is necessary in order to predict the response of a structure that has suffered fracture. Because of the complexity of the behavior of fractured masonry, perfect agreement with theory cannot be expected, and only a small number of cases can be checked, but some success has been achieved for reinforced masonry.

The first step in forming such a theory is to define anelastic strain. It is taken to be, simply, the strain that would remain if the stress were removed. (For definiteness, the stress path is specified as a straight line to the origin.) In the theory of plasticity, the plastic strain is the difference of the total strain, and the strain computed from the stress through the elastic law. But for fractured masonry, as discussed in the previous section, the elastic behavior can change substantially as cracking occurs. Hence, it is this modified elastic law that must be employed in calculating anelastic strain. Since our tests included several unloading paths, this information on elastic behavior is available.

With a procedure established for determining the anelastic strains, one can now look for some pattern that relates these strains to the stress state. As mentioned earlier, it was hoped that the influence of reinforcing steel would result in behavior close to that of the theory of plasticity. We have seen that the concepts of initial yield surface and subsequent loading surfaces do hold, with some modifications. So the final step is to see if the anelastic strains can be modeled as plastic strains.

In the theory of plasticity, the anelastic part of the strain is zero except on the yield or loading surfaces, and on these surfaces is determined only in direction, with the magnitude left undetermined. This direction is specified by the flow rule. Our tests have shown essentially elastic behavior below the loading surfaces, so it remains to find a flow rule.

Plasticity theories frequently employ an associated flow rule - one that is derived from the yield surface [18]. For many materials the increment of plastic strain is approximately normal to the yield or loading surface. More specifically, it is the increment of plastic strain whose inner product with the stress represents work, that is normal to the surface. Thus, if the surface is expressed in the stress space $(\sigma_{11}, \sigma_{22}, \sigma_{12})$, the vector $(de^p_{11}, de^p_{22}, 2de^p_{12})$ is normal to the surface.

As explained above, though, these surfaces have not been completely determined for masonry. Only a plane section through the initial yield and loading surfaces has been checked by experiment. However, the part of the surface where tests were conducted is believed to be given by Eq. (4.4), so the flow direction was compared to its normal.

The normal direction is given by the gradient of a function that is constant on the surface represented by Eq. (4.4), for example $f(\sigma_{ij}) = 0$, where

$$f(\sigma_{ij}) = \sigma_{12}^2 + \frac{\sigma_t'}{\left(1 + \frac{\sigma_t'}{\sigma_c'}\right)^2} \left(1 + \frac{\sigma_{11} + \sigma_{22}}{\sigma_c'}\right) (\sigma_{11} + \sigma_{22} - \sigma_t') - \sigma_{11}\sigma_{22} \; . \qquad (4.7)$$

The dependence of σ_t' and σ_c' on direction makes derivatives somewhat complicated. However, the normal direction is affected little by this anisotropy, so σ_t' and σ_c' were considered constant, giving

$$\frac{\partial f}{\partial \sigma_{11}} = \frac{\sigma_t'}{\left(1 + \frac{\sigma_t'}{\sigma_c'}\right)^2} \left(1 + \frac{2(\sigma_{11} + \sigma_{22}) - \sigma_t'}{\sigma_c'}\right) - \sigma_{22}$$

$$\frac{\partial f}{\partial \sigma_{22}} = \frac{\sigma_t'}{\left(1 + \frac{\sigma_t'}{\sigma_c'}\right)^2} \left(1 + \frac{2(\sigma_{11} + \sigma_{22}) - \sigma_t'}{\sigma_c'}\right) - \sigma_{11} \; . \qquad (4.8)$$

$$\frac{\partial f}{\partial \sigma_{12}} = 2\,\sigma_{12}$$

Dividing by the magnitude of the gradient gives a unit vector normal to the surface.

The anelastic strain increments were determined from plots of stress versus strain. As shown in Fig. 4.1, load was applied and removed in several steps, which represent convenient strain increments. The anelastic strain is the change in strain at zero load, which is easily determined for the tests shown in Fig. 4.1.

As discussed in Section 4.2, the behavior is fairly linear below the loading surface, and since the applied stresses were proportional, the loading and unloading curves are fairly straight. Thus, for tests that did not return all the way to zero load, the strain can be determined quite accurately by extrapolation.

The flow direction was calculated at several strains for a reinforced specimen at each of the three lay-up angles tested. Because the loading system was capable of applying only direct stresses, there was no way to determine the flow direction for the important case of shear stress on the crack plane. And since loading was proportional, for each specimen only a single point on the surface was investigated. For this point, the normal direction from Eq. (4.8) is simply (0, 1, 0).

The angles between this normal and the increments of plastic strain are given in Table 4.3. Though agreement is not perfect, the normal is seen to give a good indication of flow direction. Thus, the loading surface given by Eq. (4.4), along with the flow rule (4.8), comprise a plasticity model that should give a fair representation of the behavior of reinforced masonry.

4.4 Stress Rate-Total Strain Rate Law

The results of preceding sections define a model of post-fracture behavior, but for computations it is useful to have a set of equations that relate the rate of change of stress to the rate of change of total strain. These equations will be more complicated than those of standard plasticity because of the changing elastic moduli.

For convenience, let stress and strain components be identified by a single subscript:

$$\begin{bmatrix} \sigma_1 \\ \sigma_2 \\ \sigma_3 \end{bmatrix} = \begin{bmatrix} \sigma_{11} \\ \sigma_{22} \\ \sigma_{12} \end{bmatrix} \quad , \quad \begin{bmatrix} e_1 \\ e_2 \\ e_3 \end{bmatrix} = \begin{bmatrix} e_{11} \\ e_{22} \\ e_{12} \end{bmatrix} \quad .$$

Let e_2 be the tensile strain normal to the crack, and let $C_{ij}(e_2)$ be the changing elastic moduli (from Eq. (4.5)):

$$C_{ij}(e_2) = \begin{bmatrix} \dfrac{D_1}{1 - g\nu^2 \dfrac{D_0}{D_1}} & \dfrac{g\nu D_1}{\dfrac{D_1}{D_0} - g\nu^2} & 0 \\ & \dfrac{g D_0}{1 - g\nu^2 \dfrac{D_0}{D_1}} & 0 \\ \text{sym.} & & 2gG \end{bmatrix}$$

Let f be the loading function (Eq. (4.7)), let rate of change be indicated by a dot, and let the derivative with respect σ_i be indicated by a comma followed by i . Then the equations that describe behavior on the loading surface are

$$f(\sigma_i, e_2) = 0 \tag{4.9}$$

$$e_i = e_i^e + e_i^p \tag{4.10}$$

$$\sigma_i = C_{ij}(e_2)e_j^e \tag{4.11}$$

$$\dot{e}_i^p = \lambda f_{,i} \tag{4.12}$$

where λ is a changing parameter to be determined.

Take the derivative of (4.11) and use the derivative of (4.10), and (4.12):

$$
\begin{aligned}
\dot{\sigma}_i &= \dot{C}_{ij}\, e_j^e + C_{ij}\, \dot{e}_j^e \\
&= \dot{C}_{ij}\, e_j^e + C_{ij}(\dot{e}_j - \dot{e}_j^p) \\
&= \dot{C}_{ij}\, e_j^e + C_{ij}\, \dot{e}_j - \lambda\, C_{ij}\, f_{,j} \quad .
\end{aligned}
$$

Or,

$$\dot{\sigma}_i = \frac{dC_{ij}}{de_2}\, e_j^e\, \delta_{k2}\, \dot{e}_k + C_{ij}\, \dot{e}_j - C_{ij}\, \lambda\, f_{,j} \quad , \qquad (4.13)$$

where δ_{k2} is the Kronecker delta. From (4.9):

$$0 = \dot{f} = f_{,i}\, \dot{\sigma}_i + \frac{\partial f}{\partial e_2}\, \delta_{k2}\, \dot{e}_k \quad .$$

Multiply (4.13) by $f_{,i}$ and use the above equation:

$$-\frac{\partial f}{\partial e_2}\, \delta_{k2}\, \dot{e}_k = \frac{dC_{ij}}{de_2}\, f_{,i}\, e_j^e\, \delta_{k2}\, \dot{e}_k + C_{ij}\, f_{,i}\, \dot{e}_j - C_{ij}\, \lambda\, f_{,i}\, f_{,j} \quad .$$

Solve for λ:

$$\lambda = A_k\, \dot{e}_k \quad ,$$

where

$$A_k = \frac{\dfrac{dC_{ij}}{de_2}\, f_{,i}\, e_j^e\, \delta_{k2} + C_{ik}\, f_{,i} + \dfrac{\partial f}{\partial e_2}\, \delta_{k2}}{C_{ij}\, f_{,i}\, f_{,j}} \qquad (4.14)$$

Putting this expression in (4.13) gives

$$\dot{\sigma}_i = \left[\frac{dC_{ij}}{de_2} e_j^e \delta_{k2} + C_{ik} - C_{ij} f_{,j} A_k \right] \dot{e}_k \quad , \qquad (4.15)$$

which is the desired result. The partial derivatives $f_{,i}$ are given in Eq. (4.8), and

$$\frac{\partial f}{\partial e_2} = \frac{1 + \dfrac{\sigma_1 + \sigma_2}{\sigma_c'}}{\left(1 + \dfrac{\sigma_t'}{\sigma_c'}\right)^2} \left[\frac{1 - \dfrac{\sigma_t'}{\sigma_c'}}{1 + \dfrac{\sigma_t'}{\sigma_c'}} (\sigma_1 + \sigma_2 - \sigma_t') - \sigma_t' \right] \frac{d\sigma_t'}{de_2} \quad .$$

As an example of the application of this relation, consider a loading program for which $\sigma_3 = 0$ (no shear stress on the crack plane after fracture). Thus $\theta = 0$, so $\sigma_t' = \sigma_t$, and from (4.3), $\sigma_c' = \infty$. Equation (4.8) thus gives

$$f_{,1} = 0$$

$$f_{,2} = \sigma_t - \sigma_1$$

$$f_{,3} = 0 \quad .$$

Hence, from (4.14),

$$A_2 = \frac{\dfrac{dC_{2j}}{de_2} f_{,2} e_j^e + C_{22} f_{,2} + \dfrac{\partial f}{\partial e_2}}{C_{22} f_{,2}^2} \quad ,$$

and if $\sigma_1 = 0$, $\dot{e}_1$ should be small, then from (4.15),

$$\dot{\sigma}_2 = \frac{d\sigma_t}{de_2}\,\dot{e}_2 \quad ,$$

where $d\sigma_t/de_2$ is given by Eq. (4.1). The loading path represented by this result, together with several unloading paths from (4.5), are shown in Fig. 4.11. It compares well with the experimental result of Fig. 4.1.

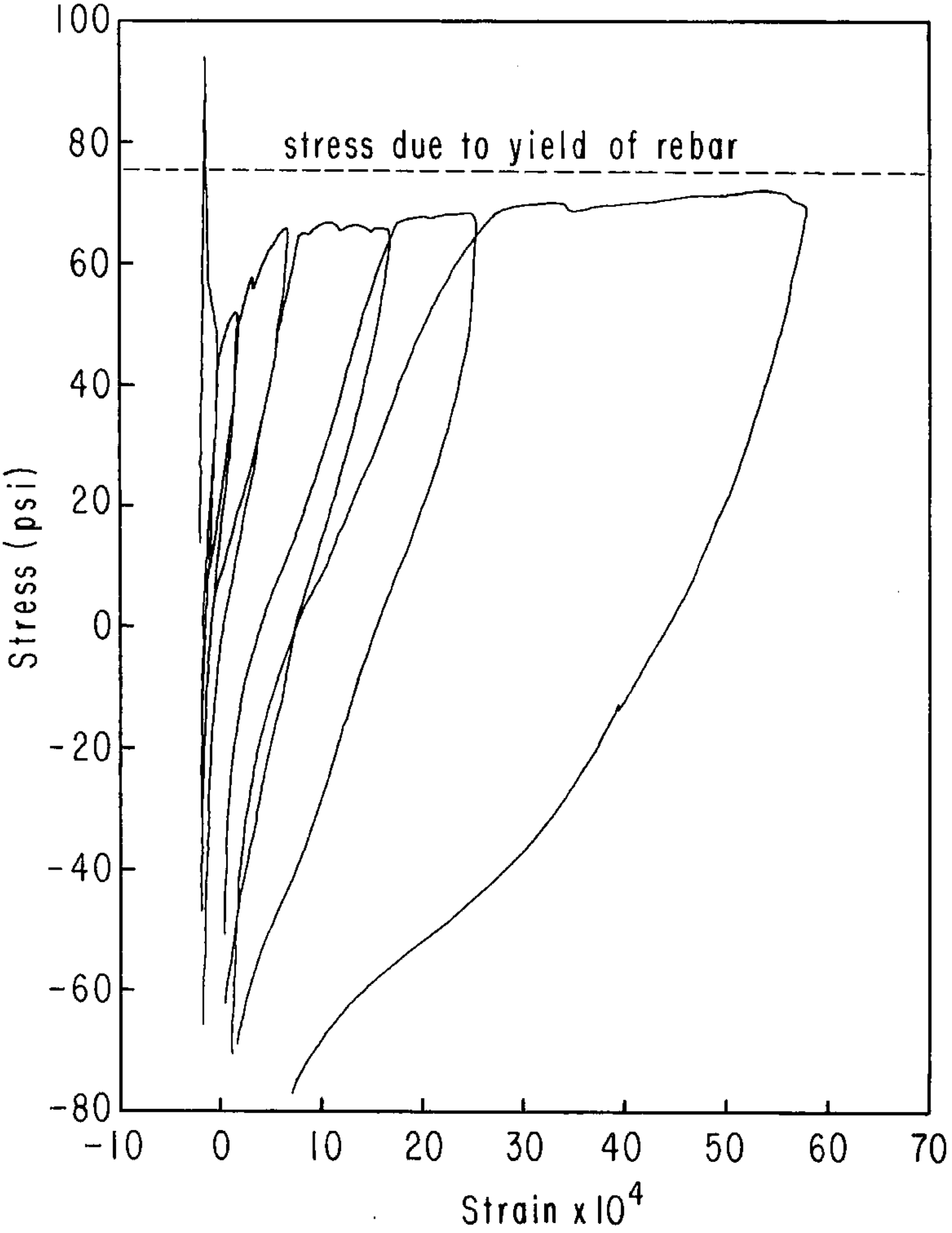

Fig. 4.1. Reinforced 0° Uniaxial Test-Large Strain

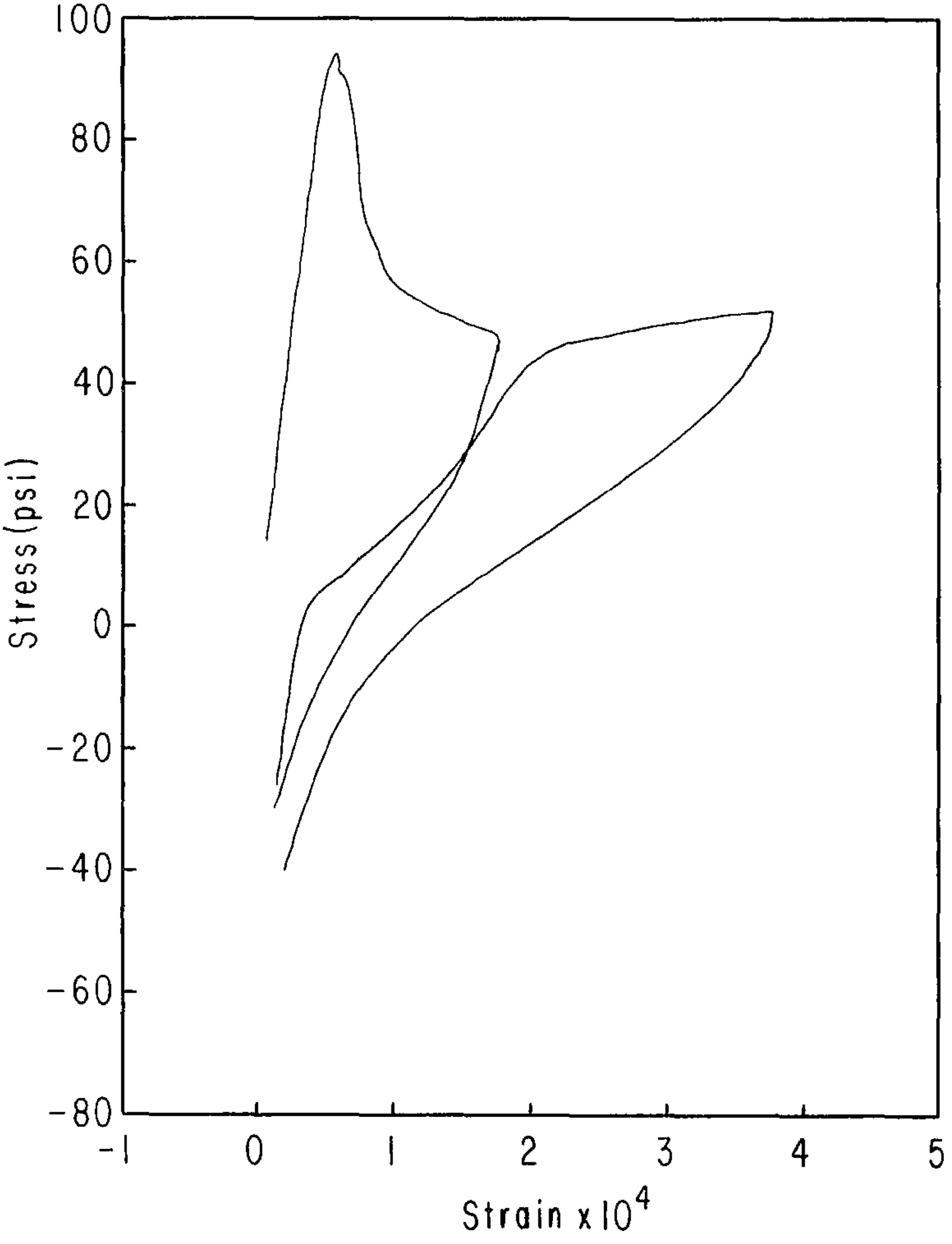

Fig. 4.2. Reinforced 0° Uniaxial Test-Small Strain

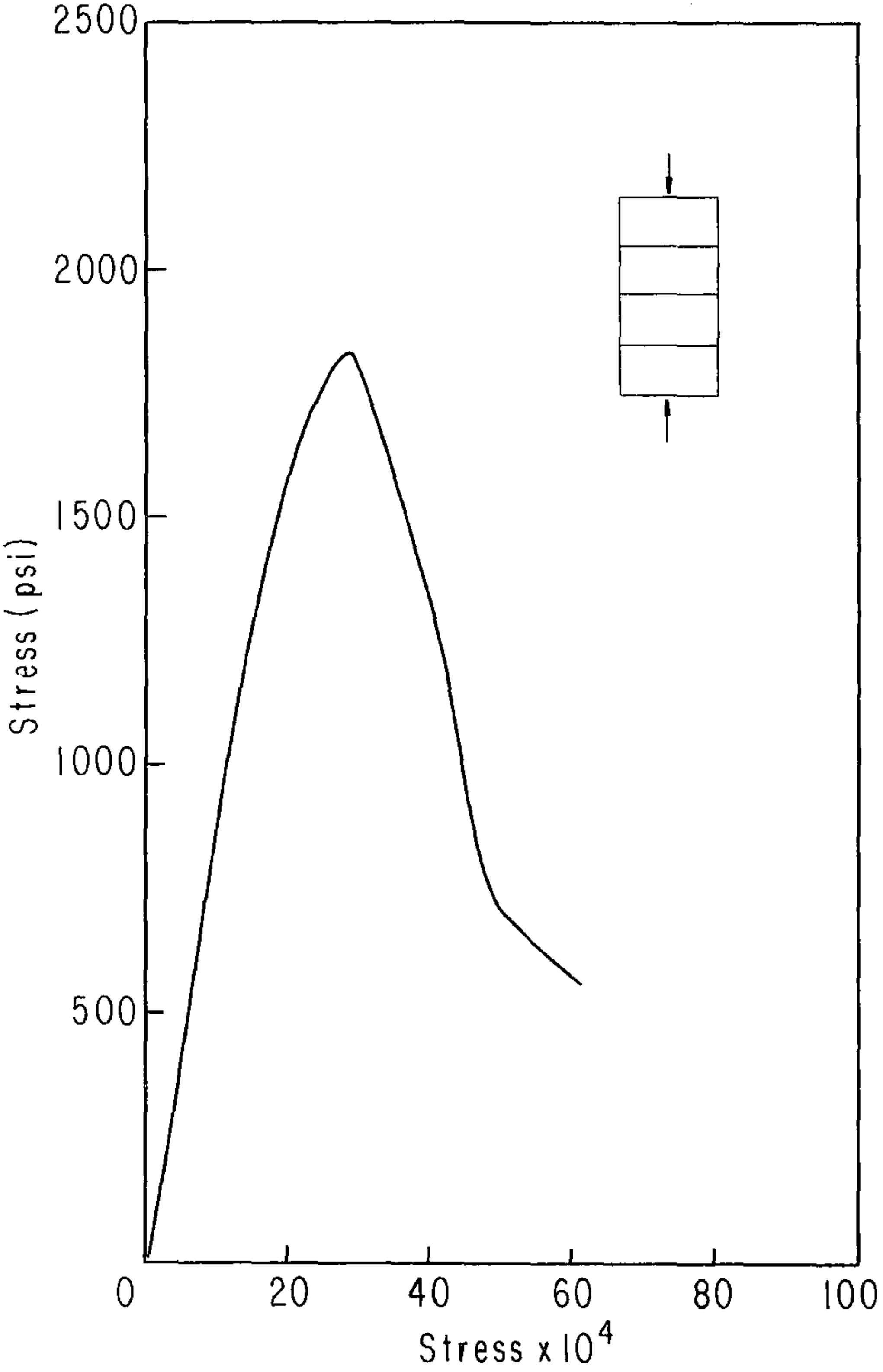

Fig. 4.3. Four-Course Stack-Bond Prism Test

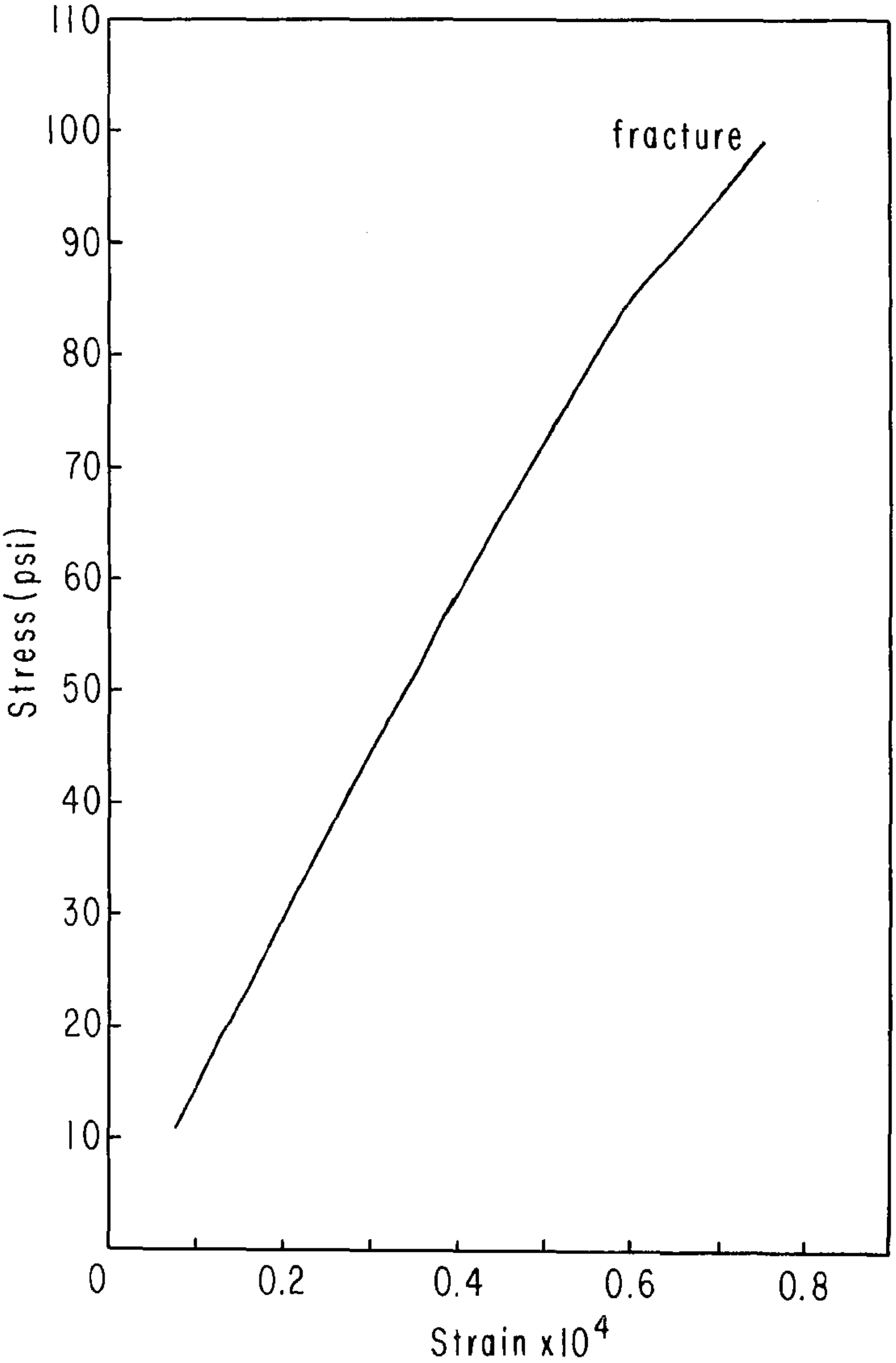

Fig. 4.4. Unreinforced 0° Uniaxial Tension Test

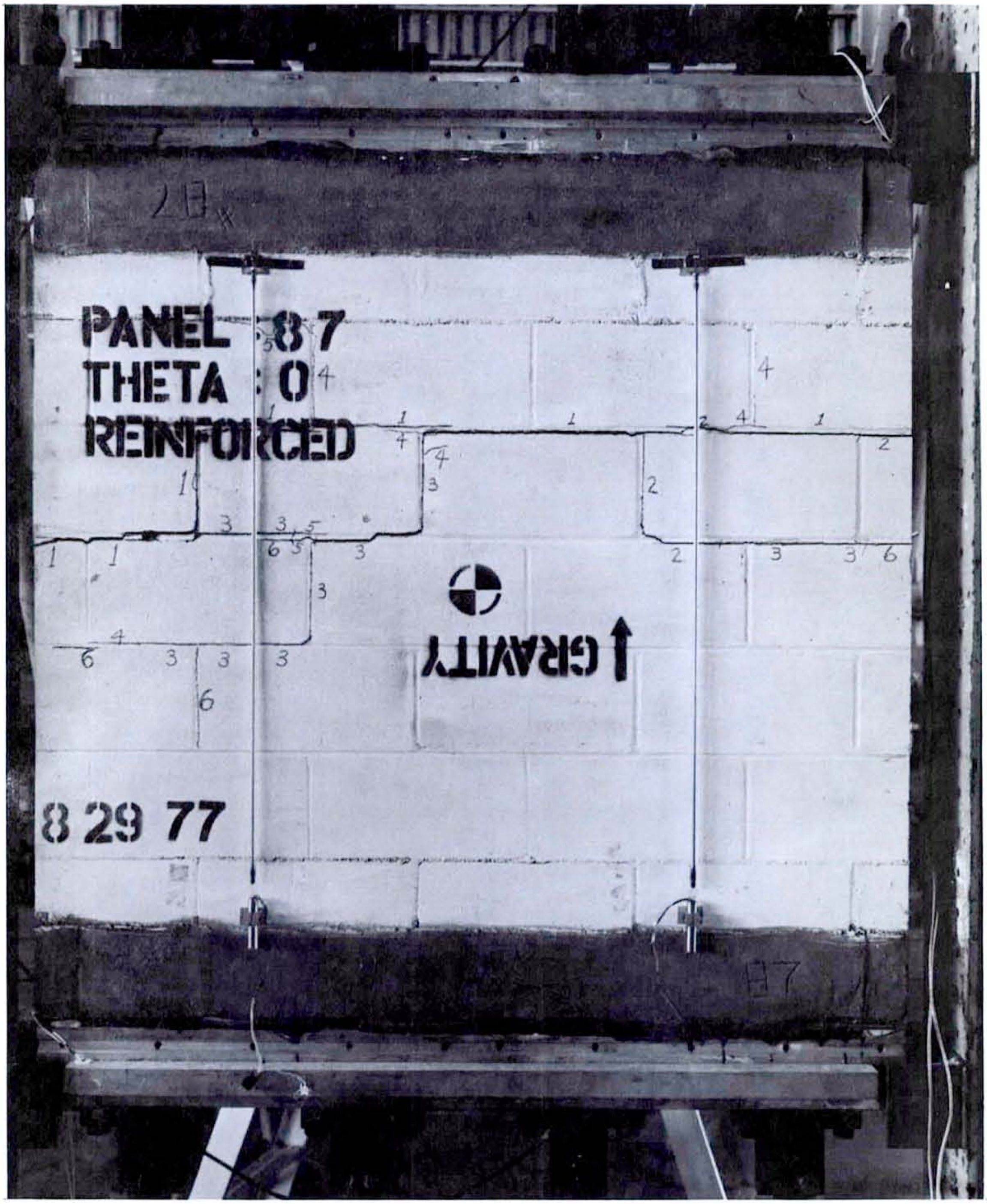

Fig. 4.5. Reinforced 0° Uniaxial Specimen

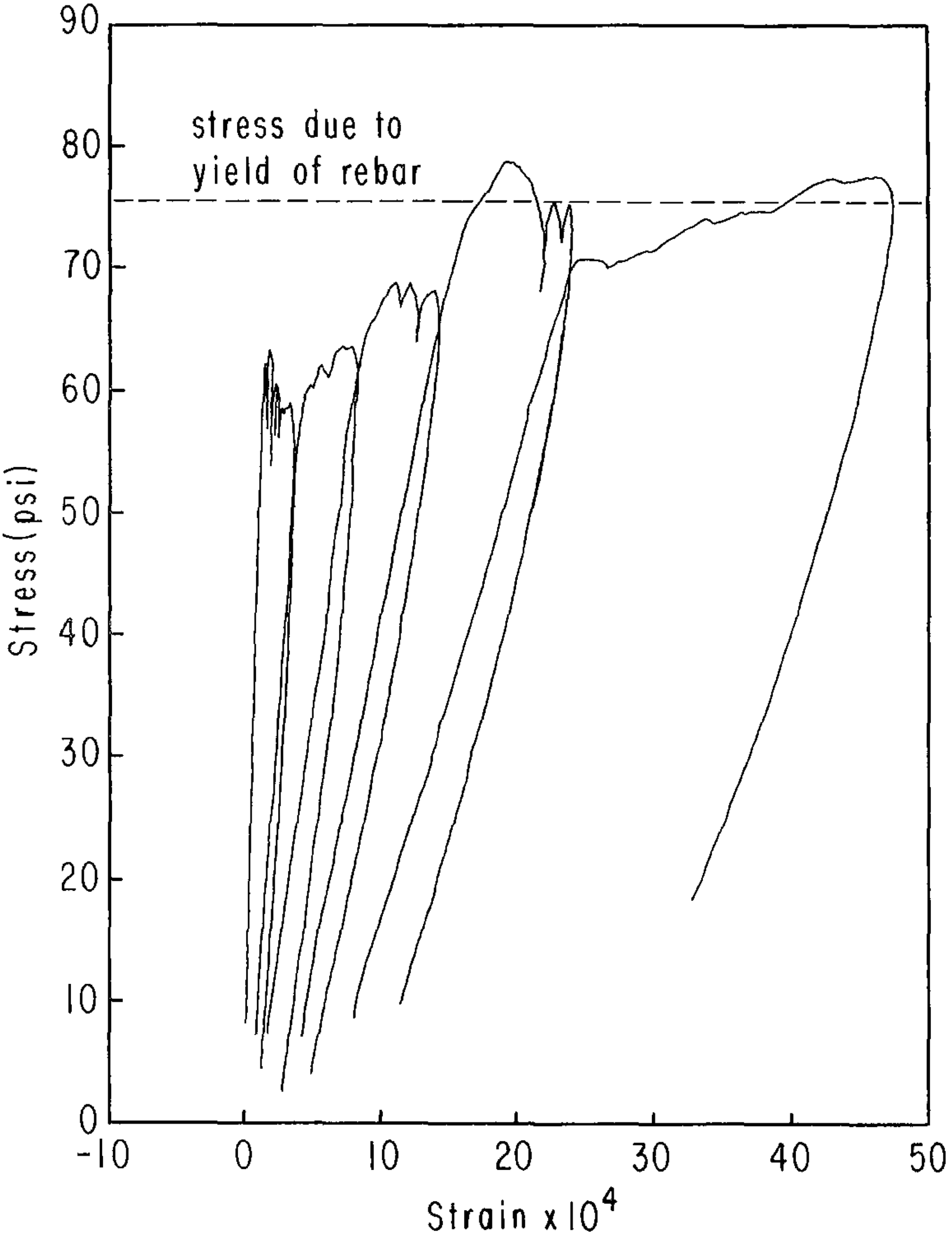

Fig. 4.6. Reinforced 45° Biaxial Test

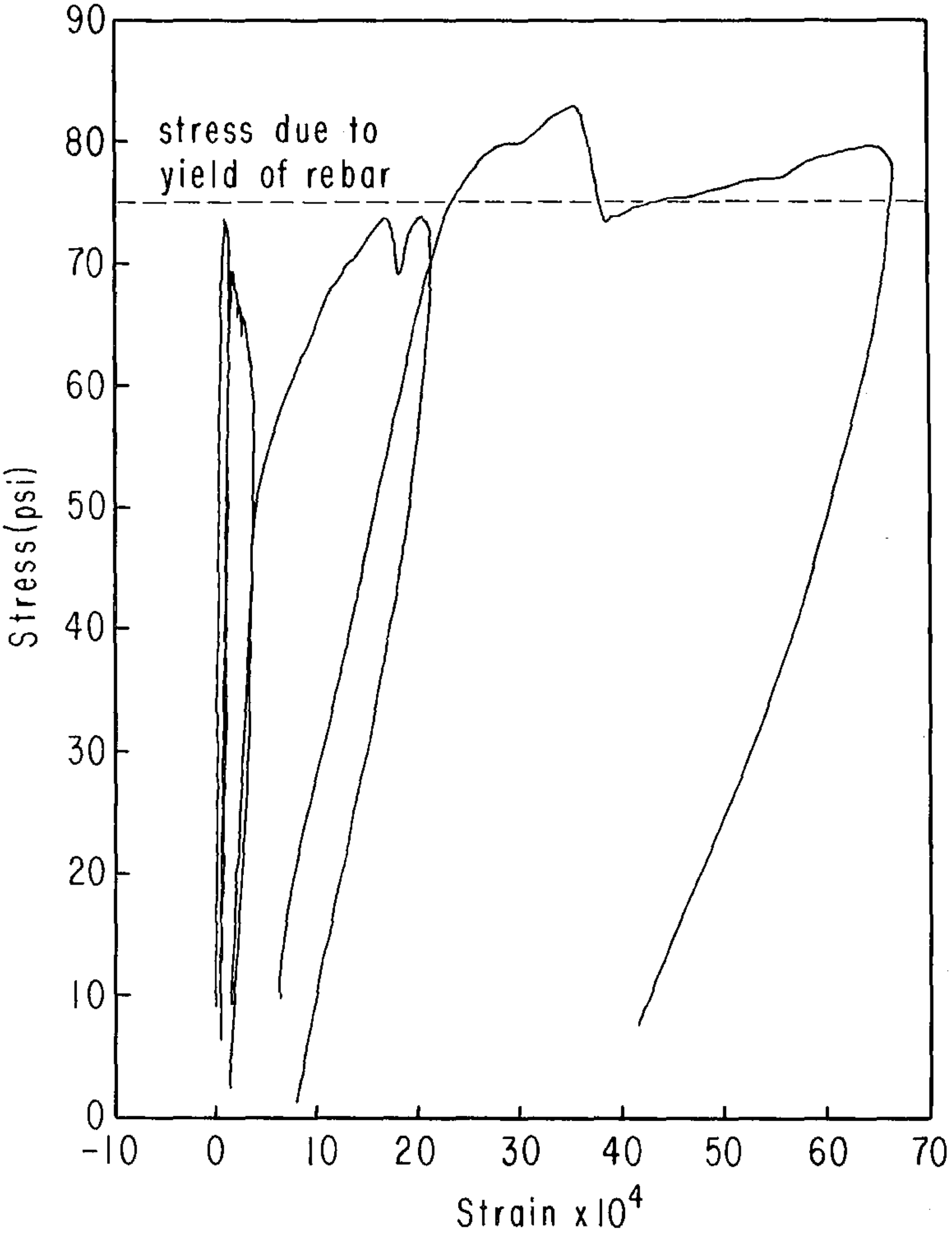

Fig. 4.7. Reinforced 70° Biaxial Test

Fig. 4.8 Reinforced 70° Biaxial Specimen

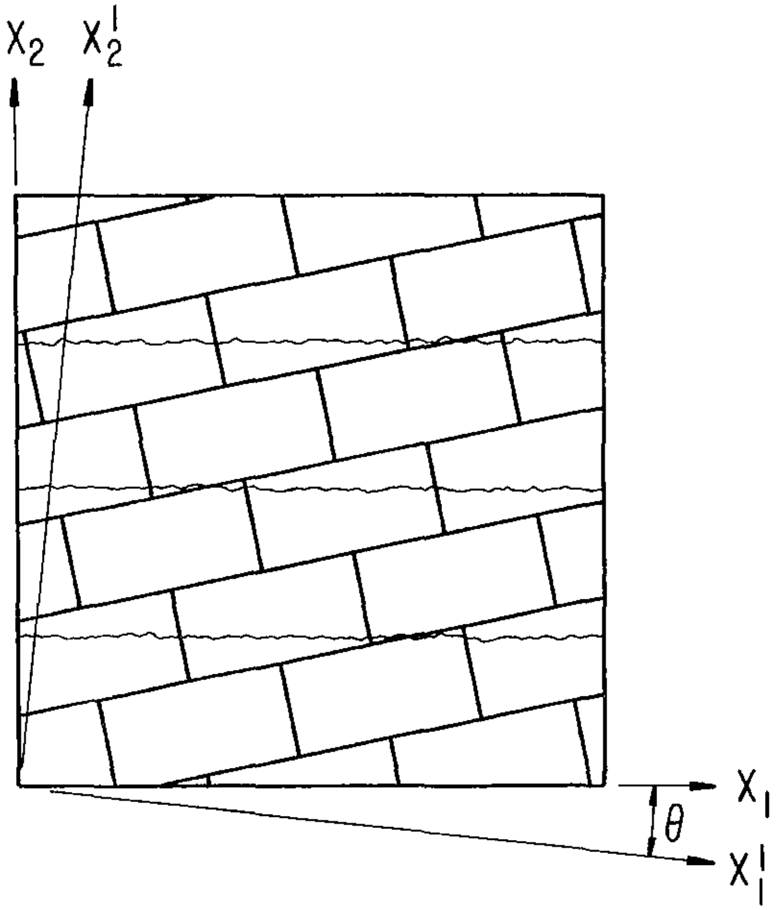

Fig. 4.9. Principal Stress and Crack Coordinate Systems

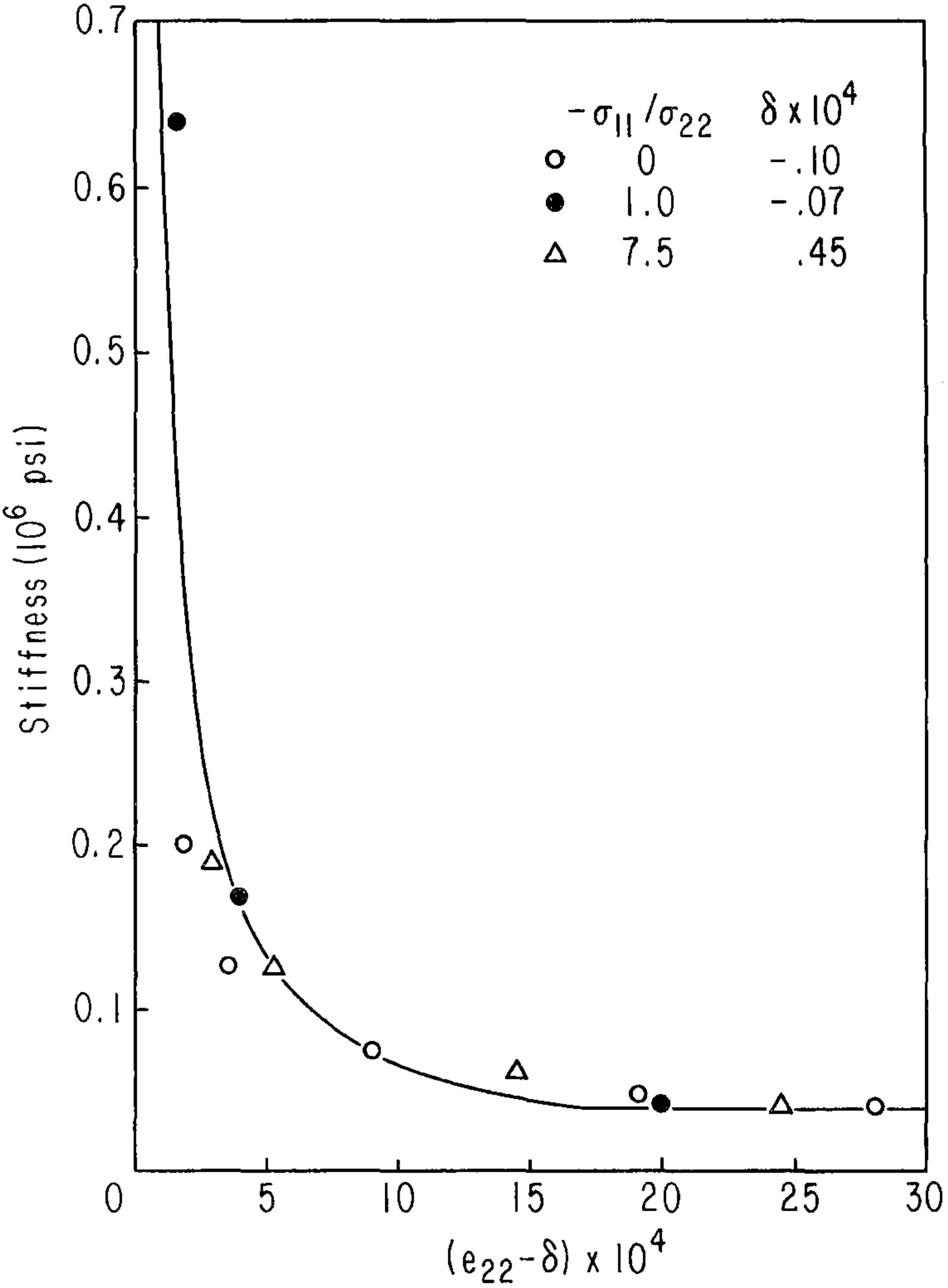

Fig. 4.10. Rate of Stiffness Degradation

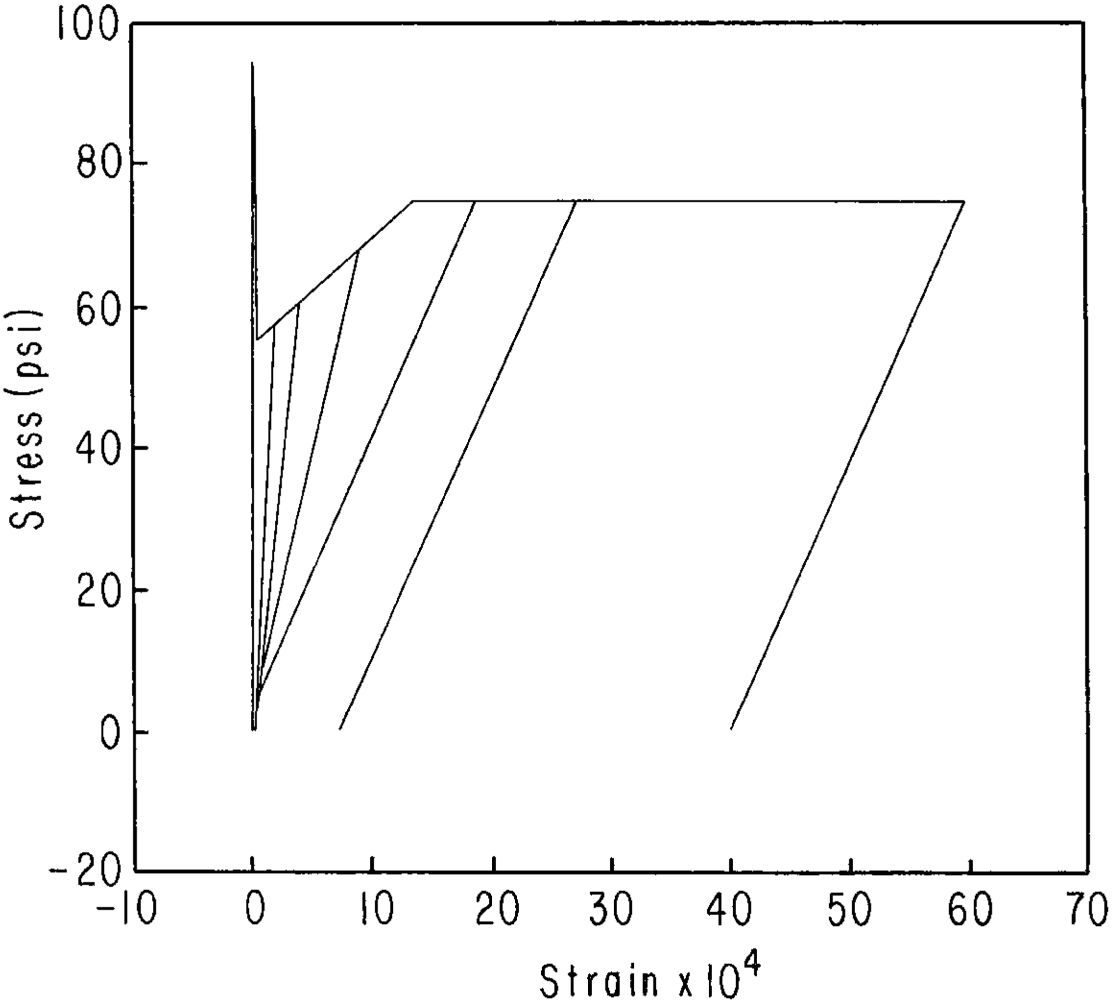

Fig. 4.11. Analytical Loading Path for $\sigma_{11} = 0$

Table 4.1. Strain Offsets for Stiffness Curve

$-\sigma_{11}/\sigma_{22}$	0	1	7.5
$(e_{22})_{\text{frac.}} \times 10^4$	0.50	0.93	1.30
$g D_0$ (10^6 psi)	1.08	0.65	0.77
$\delta \times 10^4$	-0.10	-0.07	0.45

Table 4.2. Measured Stiffnesses

	$-\sigma_{11}/\sigma_{22} = 0$				
$e_{22} \times 10^4$	1.8	3.5	9	19	28
stiffness (10^4 psi)	20.0	12.6	7.4	4.9	4.0
	$-\sigma_{11}/\sigma_{22} = 1$				
$e_{22} \times 10^4$	1.6	4.0	2.0		
stiffness (10^4 psi)	64	16.8	4.0		
	$-\sigma_{11}/\sigma_{22} = 7.5$				
$e_{22} \times 10^4$	3.5	8.0	15	25	
stiffness (10^4 psi)	18.8	8.7	6.0	3.9	

Table 4.3. Angle between Plastic Strain Increment and Normal to Loading Surface

θ	Stress Ratio	Tensile Strain × 10^4	Angle
0°	0	7	4°
		13	1°
		20	7°
45°	1.0	1.6	11°
		4	40°
		20	28°
		70	4°
70°	7.5	3.6	16°
		8	30°
		22	30°
		60	36°

REFERENCES

1. Wiegel, Robert L., coordinating editor, Earthquake Engineering, Prentice-Hall, Englewood Cliffs, N.J., 1970, pp. 167-226.

2. Hegemier, G. A., et al., "A Major Study of Concrete Masonry Under Seismic-Type Loading," Report No. AMES-NSF TR-77-002, University of California, San Diego, 1978.

3. Hegemier, G. A., et al., "Behavior of Concrete Masonry Under Biaxial Stresses," Proc. North American Masonry Conference: (1-1)(1-28), University of Colorado, Aug. 1978.

4. Nunn, R. O., et al., "Grout-Block Bond Strength in Concrete Masonry," Proc. North American Masonry Conference: (3-1)(3-9), University of Colorado, Aug. 1978.

5. Hegemier, G. A., et al., "On the Behavior of Joints in Concrete Masonry," Proc. North American Masonry Conference:(4-1)(4-21), University of Colorado, Aug. 1978.

6. Miller, M. E., et al., "The Influence of Flaws, Compaction, and Admixture on the Strength and Elastic Moduli of Concrete Masonry," Proc. North American Masonry Conference: (17-1)(17-17), University of Colorado, Aug. 1978.

7. Hegemier, G. A., et al., "Prism Tests for the Compressive Strength of Concrete Masonry," Proc. North American Masonry Conference: (18-1)(18-17), University of Colorado, Aug. 1978.

8. Arya, S. K., and G. A. Hegemier, "On Nonlinear Response Predictions of Concrete Masonry Assemblies," Proc. North American Masonry Conference: (19-1)(19-24), University of Colorado, Aug. 1978.

9. Mayes, Ronald L., et al., "Cyclic Shear Tests of Masonry Piers, Volume 1 - Test Results," Report No. EERC 76-8, University of California, Berkeley, May 1976.

10. Timoshenko, S. P., and J. N. Goodier, Theory of Elasticity, third edition, McGraw-Hill, New York, 1970, pp. 17-19.

11. Hegemier, G. A., et al., "Prism Tests for the Compressive Strength of Concrete Masonry," Report No. AMES-NSF TR 77-1, University of California, San Diego, 1977.

12. Fung, Y. C., Foundations of Solid Mechanics, Prentice-Hall, Englewood Cliffs, N. J., 1965, pp. 347-349.

13. Vierck, R. K., Vibration Analysis, International Textbook Co., Scranton, Pennsylvania, 1967, pp. 64-67.

14. 1977 Masonry Codes and Specifications, printed and distributed by the Masonry Industry Advancement Committee, April 1977.

15. Kupfer, Helmut B., and Kurt H. Gerstle, "Behavior of Concrete under Biaxial Stresses," Journal of the Engineering Mechanics Division, ASCE, 1973, pp. 853-866.

16. Walpole, R. E., and R. H. Myers, Probability and Statistics for Engineers and Scientists, second edition, Macmillan, New York, 1978, pp. 282-291.

17. Benjamin, J. R., and H. A. Williams, "The Behavior of One Story Brick Shear Walls," Journal of the Structural Division, ASCE, V. 84, 1958, pp. 1723-1 to 1723-30.

18. Goodier, J. N., and P. G. Hodge, Jr., Elasticity and Plasticity, Wiley, New York, 1958, pp. 57-61.